THESIS FOR THE DEGREE OF LICENCIATE OF ENGINEERING

Effects of pyrolysis and incineration on the chemical composition of Li-ion batteries and analysis of the by-products.

Gabriele Lombardo

Industrial Materials Recycling
Department of Chemistry and Chemical Engineering
CHALMERS UNIVERSITY OF TECHNOLOGY
Gothenburg, Sweden 2019

Effects of pyrolysis and incineration on the chemical composition of Li-ion batteries and analysis of the by-products.

Licentiatuppsatser vid Institutionen för kemi och kemiteknik
Chalmers tekniska högskola.
Nr 2019:04

Chalmers University of Technology
Nuclear Chemistry/Industrial Materials Recycling
Department of Chemistry and Chemical Engineering
Kemivägen 4
SE - 412 96 Göteborg
Sweden
Phone: +46 (0)31 772 2856 (work)
Cell: +46 (0)70 248 62 89
E-Mail: gablom@chalmers.se

Cover:
Two batteries cells (left), untreated sample obtained by pressing a puncher, with a circular diameter of 2 mm, through an equal number of cathodes and anodes (right).

Chalmers Reproservice
Göteborg, Sweden 2019.

Effects of pyrolysis and incineration on the chemical composition of Li-ion batteries and analysis of the by-products.

Gabriele Lombardo

Nuclear Chemistry/Industrial Materials Recycling
Department of Chemistry and Chemical Engineering
Chalmers University of Technology

Abstract

In the present work, the effects of pyrolysis and incineration on the composition of Li-ion battery cell materials and their dependence on treatment time and temperature were investigated. Waste from Li-ion batteries was treated at 400˚, 500˚, 600˚, and 700˚C for 30, 60, and 90 minutes. Thermodynamic calculations for the carbothermic reduction of the active materials LiCoO2, LiMn2O4, and LiNiO2 by graphite and the gas products were performed, and the results compared with the experimental data obtained by processing the pure oxides. This allowed for a very exact investigation of the behaviour of the oxides and has brought novel knowledge to the processing of Li-ion batteries. Moreover, to determine the behaviour of the real waste, NMC cathode material recovered from spent Li-ion batteries was studied. The results indicate that the organic compounds and the graphite are oxidized, by oxygen from the active material during the pyrolysis, and during incineration by the oxygen in the air present in the system, forming an atmosphere rich in CO(g) and CO2(g). Removal of the organic components increases the purity of the metal-bearing material. During the pyrolysis, reactions with C and CO(g) led to a reduction of metal oxides, with Co, CoO, Ni, NiO, Mn, Mn3O4, Li2O, and Li2CO3 as the main products. The reduction reactions transformed the metal compounds in the untreated LiB black mass into chemical forms that were more soluble. It was concluded that pyrolysis can be used as an effective tool for pre-treatment of battery waste in order to increase the efficiency of leaching in a hydrometallurgical processing of the black mass. During incineration, it was observed that the organic material was removed more efficiently than in pyrolysis and the lithium metal oxides were subjected to both carbothermic reduction and oxidation. During heat treatment, organic by-products were formed by the decomposition of the polypropylene separator and the PVDF binder. The organic residue contained both non-polar and polar compounds. One of the most important outputs of the current work is the observation of the fluorine behaviour during the thermal treatment, and

detection of its presence in the oil product. It was shown that the decomposition of the PVDF facilitates the separation of the active material from the metallic layers of the electrodes by means of a mechanical treatment. An almost complete recovery of the black mass from the foils was achieved following the thermal treatment. The results obtained can help to optimize the parameters in the industrial process that is already used for Li-ion battery recycling, since this research provides novel information about the effects of the thermal treatment and defines the most favourable conditions for the processing. The results could contribute to an increased recycling rate, especially if this process is followed by a hydrometallurgical treatment. Such optimization will decrease the energy demand and increase the metal recovery rate and the utilization of the by-products.

Contents

f

1. Introduction

Lithium-ion batteries (LiBs) are now the most widely used power source for portable electronic devices, because they can provide high energy and power per unit of battery weight, which means that they can be made lighter and smaller than other rechargeable batteries [1]. Due to its performance, the LiB is also widely employed in the car industry for fully electric and hybrid engines [2] [3]. About 95% of the global market for electric cars is located in just ten countries: China, United States, Japan, Canada and Europe (Norway, United Kingdom, France, Germany, the Netherlands, and Sweden) [4]. In 2017, global sales of electric cars reached 1.1 million, with an increase of 54% compared to 2016. China has half of the global electric car market, with nearly 580,000 electric cars sold there in 2017, while the European Union and the United States each accounted for about a quarter of the global total. The International Energy Agency estimates that the demand for LiBs is rising: the global electric car stock passed the 1 million mark in 2015, 2 million in 2016, and exceeded 3 million vehicles in 2017 (Figure 1). The forecast indicates that there is a good chance that the number of electric vehicles will range between 9 million and 20 million by 2020, and between 40 million and 70 million by 2025 [5][6].

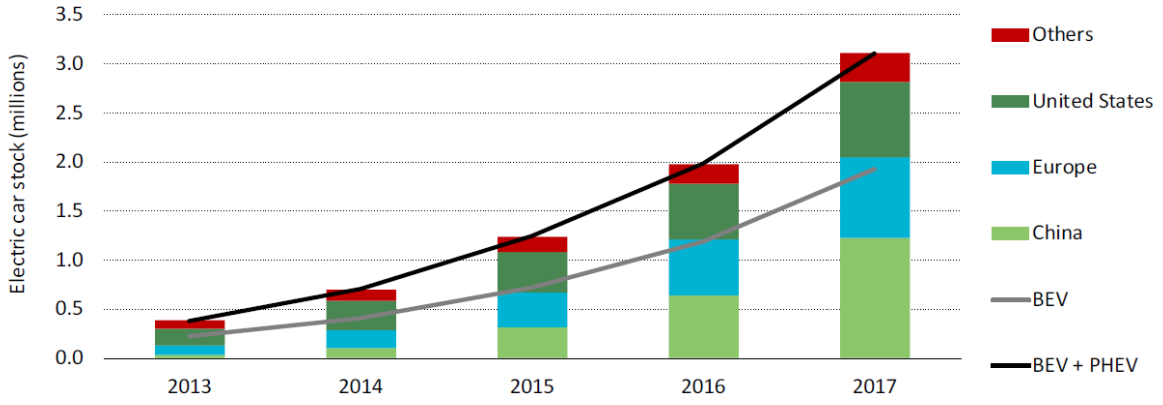

Figure 1: Evolution of the global electric car stock 2013-17. BEVs: Electric vehicles including battery electric vehicles; PHEVs: plug-in hybrid electric vehicles. Sources: IEA analysis based on country submissions, complemented by ACEA (2018); EAFO (2018).

The increasing use of LiBs is causing simultaneous rapid growth in the demand for the metals necessary for their production, in particular cobalt (Co), nickel (Ni), manganese (Mn), and lithium (Li). If this trend continues, the current reserves of Co will be depleted in less than 60 years [7]. Co is already one of the critical raw materials, as can be observed in Figure 2, due to its economic importance and supply risk [8]. In addition, cobalt mining in some countries is associated with serious negative impacts on the environment and also with negative social impacts, such as child labour.

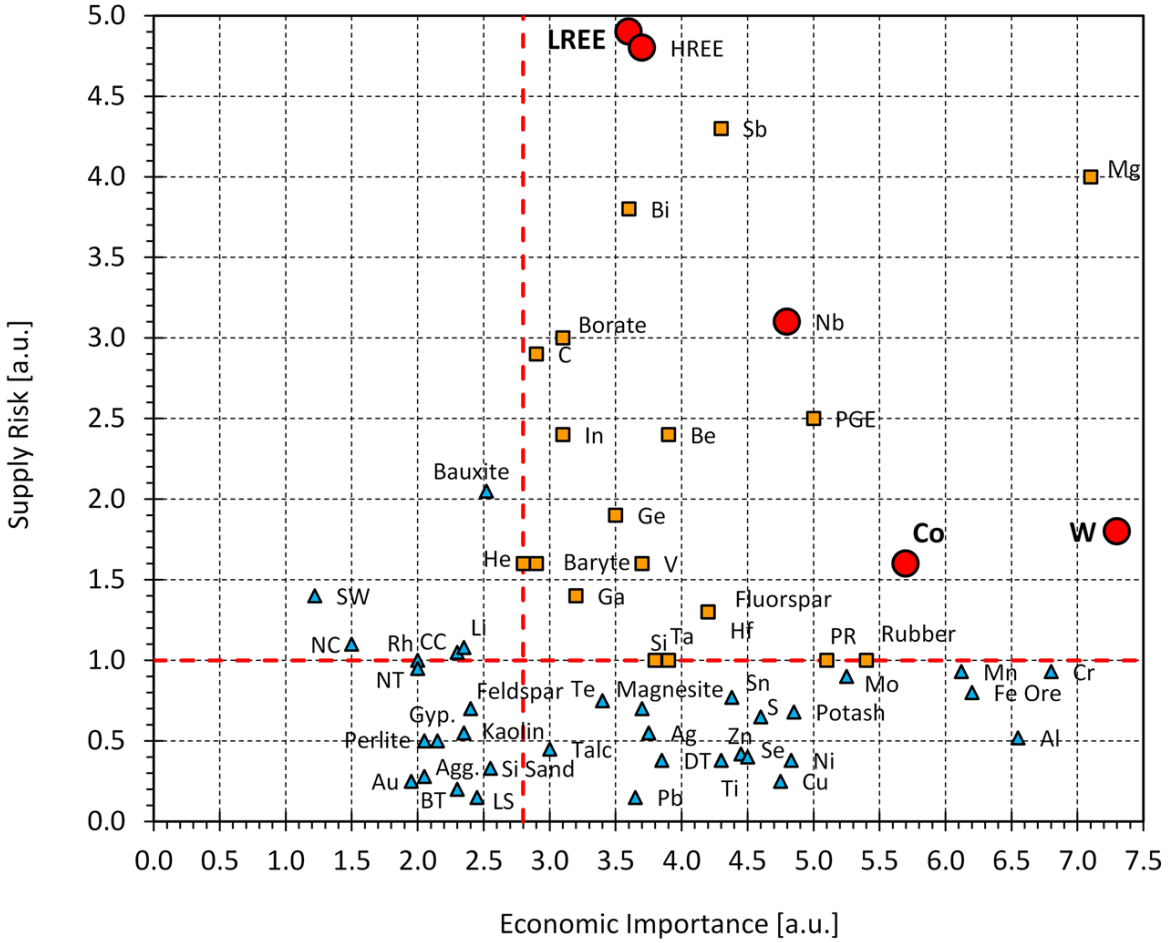

Figure 2: The list of critical raw materials for the EU 2017 [8].

For Li, no real scarcity is foreseen until 2050, by when the easily extractable lithium reserves in stable countries might decrease significantly. On the other hand, its price has already increased fourfold since 2015 [9]. The resources of this light metal are concentrated in a few countries, mainly Chile, followed by Bolivia, China, and Argentina. Its mining has historically been associated with different forms of institutional risk, such as uncertain mineral rights, conflicting land use, security risks, and other political exposure. This influence is creating instability in the supply and price of Li [9]. Nickel is expected to be less impacted by the increasing use of LiBs than is the case for the other materials. The annual production is around 2000 kilotons, which primarily satisfies the demand for steel production; batteries account for a small fraction of the total. Furthermore, an oversupply was seen that lasted up to 2015 [2]. Another critical raw material is the graphite [8], commonly used as anode active material in commercial LiBs. The type of natural graphite used for the production of batteries is mainly supplied by a few countries (China, Canada, and Madagascar) and has a limited availability

(Figure 3). Petroleum coke and coal tar pitch are thermally treated at high temperature to produced synthetic graphite but, due to its high cost, its application is limited [10].

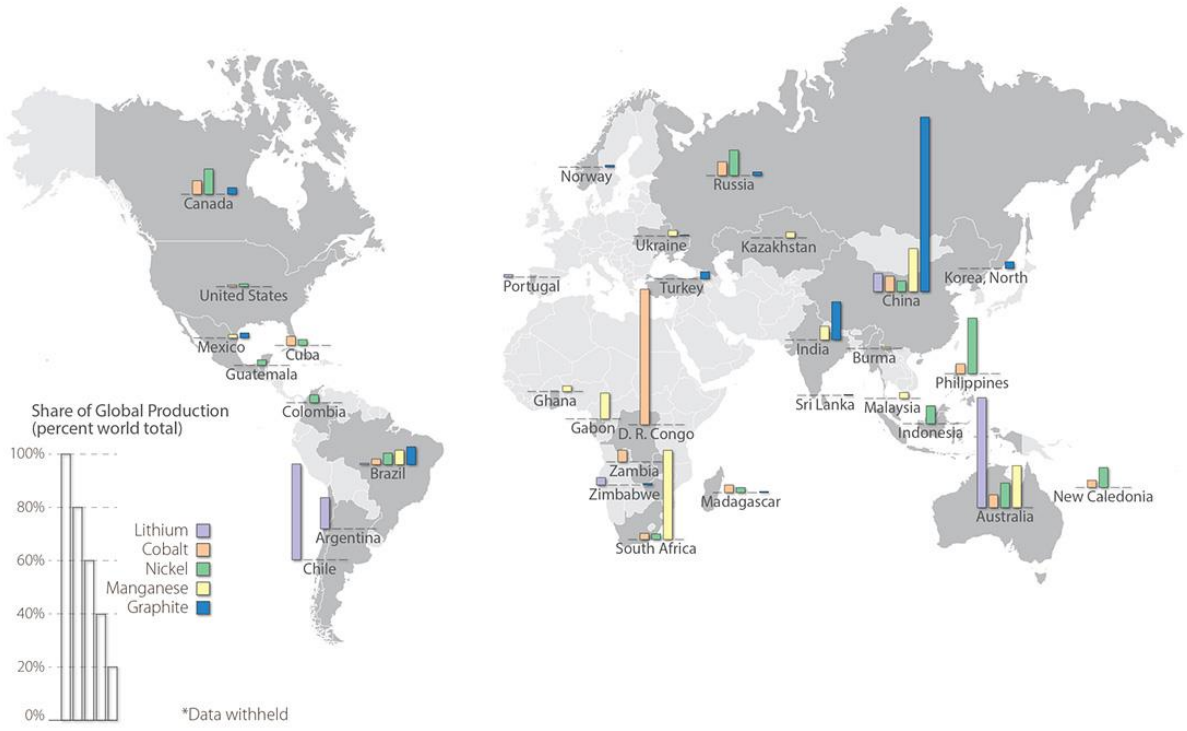

Figure 3: Distribution of the mineral resources for some of the main elements present in lithium batteries: Source: Clean Energy Manufacturing Analysis Center (CEMAC).

Due to the forecasted increasing demand for LiBs raw materials, the critical reserves of Co and the instability in supply and price of Li, it is important to develop efficient and cost-effective recycling methods for LIB materials.

The recycling of spent batteries could provide a solution for overcoming shortages in resource supply and the dependency on temporary price fluctuations on the global market. The metals that are economically interesting, and most in focus for recycling efforts, are concentrated especially in the active material and in the collecting foils. However, the recycling processes used at present are focused on recovering Co and Ni, not Li. The increasing demand for LiBs will make it necessary to include the recycling of Li as well, to ensure long-term sustainability of the LiB technology [1] [9].

Hydrometallurgical recycling of the metals in the active materials of LiBs offers a possibility that Li could be recovered during the process. Rather high operating costs for the hydrometallurgical routes and the need for mechanical pre-treatment are the main disadvantages. A thermal pre-treatment might be a solution for further improving the

hydrometallurgical recycling route. This kind of treatment is optimized primarily for removing graphite and organic compounds, especially since the binder can cause problems during leaching and solvent extraction, but it can also have important effects on the composition of the active material and improve the recovery of metals in the following hydrometallurgical methods. Therefore, the aim of this work was to study and compare the effects of pyrolysis and incineration, as thermal pre-treatments, on the composition of the battery cell materials as a function of treatment time and temperature.

This was performed by pyrolysis and incineration of NMC-LiBs, i.e. batteries in which the cathode's active material generally has the composition $Li(Ni_xMn_yCo_z)O_j$. In a thorough literature review, no published investigations were found in which the effects of high temperature on a mixture of both the cathode and anode materials of a commercial NMC battery were examined. The study of these effects is crucial for understanding if thermal pre-treatment can further improve the recovery of metals in the following hydrometallurgical methods. It was expected that during the pyrolysis the carbon present in the battery would trigger a carbothermic reduction of the metal oxides of the cathode's active material. Co, Ni, Li, and Mn compounds would be reduced to a lower oxidation and/or more soluble state, and so improve the leaching efficiency. It was also expected that the metallic Cu and Al would not be oxidized and, therefore, they could be separated from the rest of the black mass. In this way, it would be possible to avoid the initial mechanical separation of the electrodes and the addition of a reducing agent during the leaching.

The incineration was expected, instead, to cause the complete oxidation of the Cu and Al layers and a different decomposition of the lithium-transition-metal-oxide, with the formation of more oxidized species.

At the same time, it was expected that the high temperature would result in an increase in the kinetics of the decomposition of the battery's organic components, with the formation of by-products.

2. Background

A lithium-ion battery (LiB) is consists of five principal components: anode, cathode, separator, electrolyte and current collector (Figure 4).

The negative electrode (anode) consists of a Cu foil coated with graphite. In the lithium-ion battery, the charging and discharging events are determined by the movement of the lithium cations from the cathode to the anode and vice versa. During charging, the Li ions move from the cathode material through the electrolyte to the separator and then again through the electrolyte to the anode. This event creates a flow of current up the copper current collector and to the positive current collector. During the charging/discharging cycles, Li ions have to intercalate and de-intercalate reversibly in the framework of the active material without introducing any significant structural changes.

The positive electrode (cathode) is an Al foil covered with an electrochemically active material, the chemistry of which is dependent on the application for which the various kinds of lithium batteries are produced [11]. In the batteries used in the automotive field, the active material coated on the cathode is generally a lithium-transition-metal-oxide ($LiMO_2$), where the metal M can be Co, Ni, Mn, Al, or one of their combinations [12] [13]. One of the most commercialized cathode materials has the general composition $Li(Ni_xMn_yCo_z)O_j$, and is known as NMC. Another common, ternary, metal active material is the NCA consisting of Ni–Co–Al oxides [1].

The adhesion between the aluminium foil and the active material is improved by a polymeric binder, most often polyvinylidene fluoride (PVDF) [14].

The electrodes are kept separate by a layer made of polypropylene (PP) or polyethylene (PE), called the separator. The properties of this layer are important, because it must be permeable to Li cations but at the same time prevent contact between the electrodes and, thus, an internal short circuit and cell failure [15].

The ion conductivity is facilitated by an electrolyte [1] [16] that represents 9-12% [17] by weight of the battery. Typical electrolytes include mixtures of alkyl carbonates [18] and Li salts, such as $LiPF_6$ [19]. The electrolyte generally includes a set of additives that provide different effects, firstly they act to facilitate the formation of the solid electrolyte interphase (SEI) layer [20], due to the decomposition of the electrolyte, mostly during the first cycle of charge/discharge. The SEI layer is of great important for the longevity of the battery, because it prevents further electrolyte decomposition and prevent graphite exfoliation, which may be caused by solvent co-intercalation between the graphene layers.

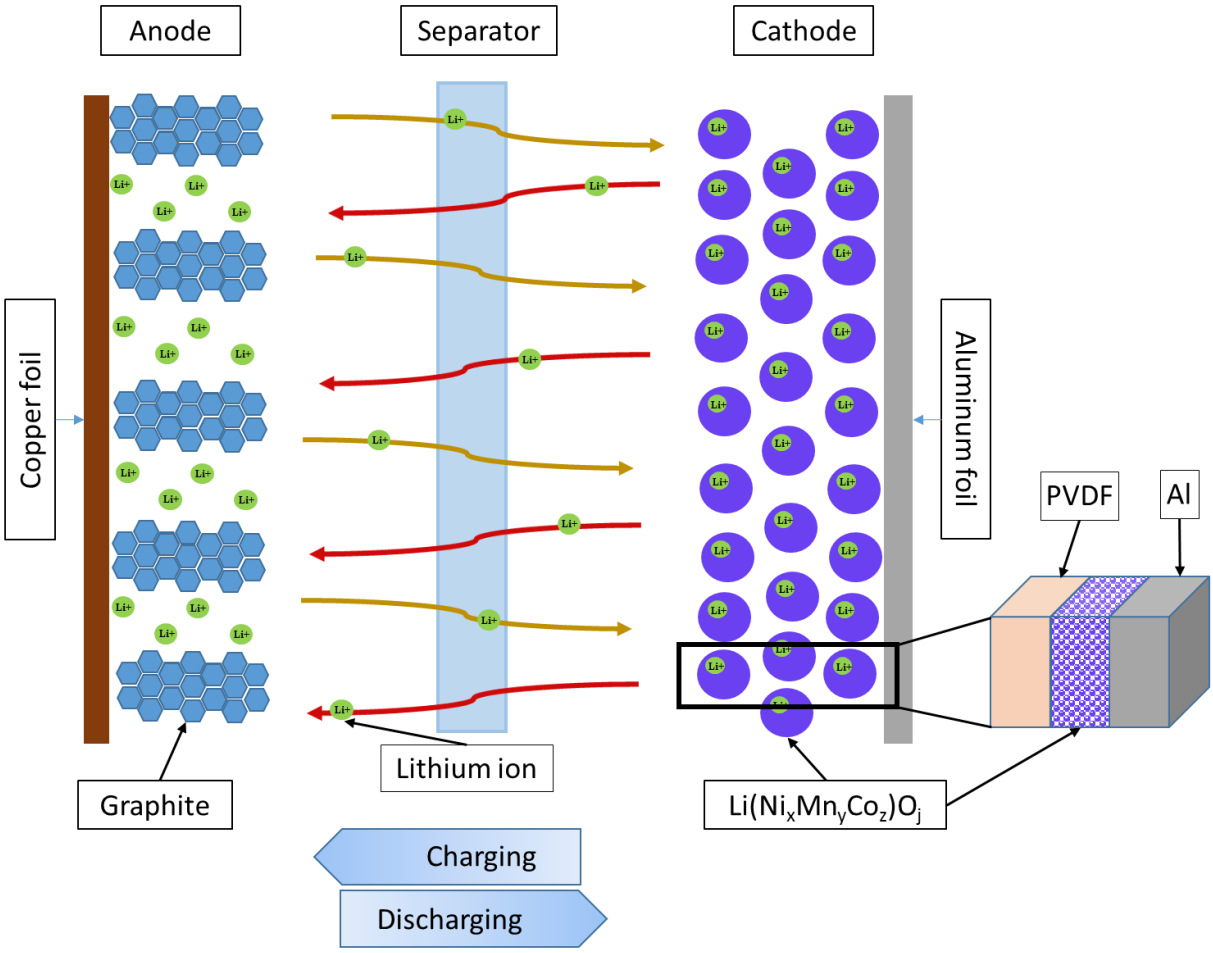

Figure 4: Principle of Li-ion battery

All of these components are inserted into a container that can be a metal can, a plastic enclosure, or a metal foil-type pouch. The electrolyte liquid is injected, and the entire assembly is hermetically sealed [1].

The battery also includes peripheral components, such as cables, casings, and electric connectors, which contain mainly plastic and copper, steel and aluminium. All of these peripheral components can be recovered using conventional recycling methods for waste electrical and electronic equipment (WEEE) [7].

2.1 Current state in the industrial recycling

To achieve the goal of high recovery rates, despite the large variety in the chemistry and hazards associated with spent LiBs, the recycling process for LiBs consists of a combination of different single operations: discharging followed by mechanical, pyrometallurgical and

hydrometallurgical treatment [15] [21]. First, the batteries are discharged to avoid short-circuits and sparks that might ignite volatile organic compounds during the crushing process. The Umicore company uses thermal preheating of the battery cells to a maximum temperature of 300°C. After this treatment, the battery cells are inactivated electrochemically [15].

After the discharge treatment, many companies continue the recycling process by means of a hydrometallurgical (Recupyl - France) or pyrometallurgical treatment (Umicore – Belgium, Nickelhutte – Germany, Sony - Sumitomo - Japan, etc.). An example of such a process, as developed by Umicore, is called ultra-high temperature (UHT) and involves using plasma technology to treat and recycle spent Li batteries. The products of this treatment are an alloy containing Co, Ni, Cu, and Fe, which are then recovered hydrometallurgically [22] [23] and an Al-Li-Mn slag, which can be used in the construction industry [24] [25]. The graphite cannot be recycled, since part of it is burned and part of it remains in the slag [1] [15]. No pre-treatment is generally needed [26].

Hydrometallurgical methods include recovery of metals from the black mass by means of leaching, solvent extraction, precipitation and/or ion exchange methods. Hydrochloric, or sulphuric acid, is used most commonly for leaching [27]. In many cases, a reducing agent is added to further increase the leaching efficiency. For example, hydrogen peroxide is added to reduce Co, Ni, and Mn compounds to species that have a higher solubility [29] [30]. The recovery of pure metals is obtained by solvent extraction processes and precipitation [29] [31]. Hydrometallurgical recycling of the metals in LiB active materials offers the possibility that Li could be recovered during the process. The addition of saturated solutions of Na salts to the Li-containing solution can be used to recover Li by precipitation, for example, as Li_2CO_3 or Li_3PO_4. In comparison to pyrometallurgy, the hydrometallurgical method has many advantages including lower energy consumption, less hazardous gas emissions, higher material recovery rates, and the ability to recycle Li, Mn and Al [32] The disadvantage is that this process is more complex, because it needs a series of additional pre-treatments to separate the different components of the batteries and to remove the organic materials. Generally, the hydrometallurgical method involves a thermal or mechanical pre-treatment to separate the cathode's active material from the aluminium foil and to remove the organic components that might inhibit leaching and solvent extraction [33]. Mechanical pre-treatment is applied to separate the different components and to recover the coating on the anode and cathode, the so-called black mass (Akkuser (Finland), Redux (Germany), Retriev Technologies (USA)). In

Retriev's plant in Ohio, the mechanical treatment is carried out using a crusher operating under a liquid solution, in order to reduce the reactivity of the processed batteries and to prevent the emission of volatile compounds [21].

2.2 State of the art of LiBs thermal treatment research

A thermal pre-treatment may provide a way to improve the hydrometallurgical recycling route further. This kind of treatment is primarily optimized for removing graphite and organic compounds, especially since the binder can cause problems during leaching and solvent extraction, but it can also have important effects on the composition of the active material and improve the recovery of metals in the following hydrometallurgical methods.

Incineration has been shown to have a high efficiency as a method for the removal of organic components, with positive effects on Co and Li leaching. A general decrease in the material weight, due to the removal of graphite and organic compounds, was noted during the thermal treatment in work done by Petranikova and co-workers [34]. A partial decomposition of the cathode material into Co_3O_4 at 500°C, and into Co_3O_4 and CoO at 700°C, was observed after 60 minutes of treatment [34]. The complete removal of the carbon content in $LiCoO_2$ batteries was obtained by Paulino and co-workers after calcination for 5 hours, with the consequence that the subsequent Li extraction increased, because carbon can absorb lithium ions and thus disrupt the extraction [35]. An improvement in Co and Li extraction after incineration at 700 °C was also reported by Petranikova et al. [34] as well as by Shin et al. [36]. A further increase in the temperature has been reported, instead, to limit the extraction due to melted aluminium foils coating the lithium cobalt oxide particles [37].

Only recently has pyrolysis been investigated as an alternative treatment method. It was observed that it is possible to remove the binder efficiently and to decompose $LiCoO_2$ into CoO and Li_2O by pyrolyzing the cathodes of $LiCoO_2$ batteries at 600˚C under vacuum for 30 min [37]. It has also been reported that, when using a higher temperature (800°C and 1000°C) in a pyrolysis process in the presence of graphite, a mixture of Co and Li_2CO_3 was obtained [38].

Xiao and co-workers [39] exposed a mixture of $LiMn_2O_4$ and graphite to a thermal treatment at 800°C in a vacuum and found that this treatment converted the electrode materials into Li_2CO_3 and MnO. The Li could then be recovered as Li_2CO_3 by leaching with water. Yang and co-workers observed that, by treating NMC-LiB cathodes at 600 °C in high purity nitrogen for

15 minutes, it is possible to completely remove the binder and separate the active material from the aluminium layer [40].

Thus, the benefits of combining pyrometallurgical and hydrometallurgical processes are evident and this is driving the majority of the current progress and research in the field of recycling. Hydrometallurgy is considered to be a technology with a smaller carbon footprint than pyrometallurgy and, moreover, it allows for the recovery of the majority of the battery components. Thermal pre-treatment helps to separate battery components and simplifies discharging the batteries. Despite such efforts, the effects of pyrolysis on a mixture of both cathode and anode materials have not been explored, even though pyrolysis is used in industrial recycling and its effect has to be determined for sustainable waste processing.

3. Materials and methods

This work was performed on lithium battery cells provided by the VOLVO CAR CORPORATION. A total of 6 cells were dismantled by removing the plastic cover. The cathodes and anodes were separated from the separators manually. The black mass was scraped from the anode copper foils and cathode aluminium foils. The separated components were weighed. The batteries were manually dismantled to conduct qualitative and quantitative analysis of the battery cells. For the pyrolysis and incineration experiments, crushed mixed battery waste with separator was used.

3.1 Thermal treatment

The plastic covers of the 6 cells were opened and removed. The electrodes were collected and representative samples were obtained by pressing a puncher, with a circular diameter of 2 mm, through an equal number of cathodes and anodes (Figure 5). Samples weighing 0.5 g were placed on an alumina holder and inserted in a quartz tube, with the dimensions 700 mm long and 30 mm diameter, with a cone 34/35 and socket 34/35. A tubular furnace, Nabertherm GmbH Universal Tube Furnace RT 50-250/11 - RT 30-200/15, was used for the thermal pre-treatment. The furnace's heating rate was set to 10ºC/min and the tube was thermally insulated. A constant flow of approximately 340 ml/min of 99.9% pure nitrogen, for the pyrolysis, or air, for the incineration, was pumped through the tube and a flow meter was used to regulate the gas flow at the entrance to the system. The exiting gas was bubbled through a glass cylinder filled with 100 ml of MilliQ water (Figure 6).

Figure 5: Untreated sample.

The samples were heated to 400, 500, 600 and 700ºC. The choice of this temperature range was the result of a compromise: at a lower temperature, the efficiency of the PVDF removal, and thus the purity of the treated black mass, should be lower than it would be when treated at a higher temperature. On the other hand, higher temperatures can cause the Al to melt (melting point 660.3 °C), which, in the liquid state could coat the samples inhibiting removal of the PVDF and the contact between the battery and the reducing atmosphere in the furnace. It was decided to perform the treatment at 700˚C to see if there were any effects due to Al melting at this temperature. To reach the desired temperature, the sample was inserted in the tube into the

centre of the furnace and kept there for 30 minutes, 60 minutes and 90 minutes respectively. After the selected heating time, the heating and the gas flow were shut down and the sample was moved near to the end, to remain in the reducing atmosphere while cooling down. The loss in sample weight was examined by weighing the samples before and after the experiment. Experiments were carried out in triplicate.

Standard samples, consisting of a mixture of graphite and one of the pure metal oxides present in the black mass ($LiCoO_2$, $LiMn_2O_4$, and $LiNiO_2$), were subjected to the same thermal treatment. These standards were analysed and compared to the NMC-LiB samples in order to identify the mechanism of decomposition for each metal oxide and, thus, confute or confirm the thermodynamic considerations.

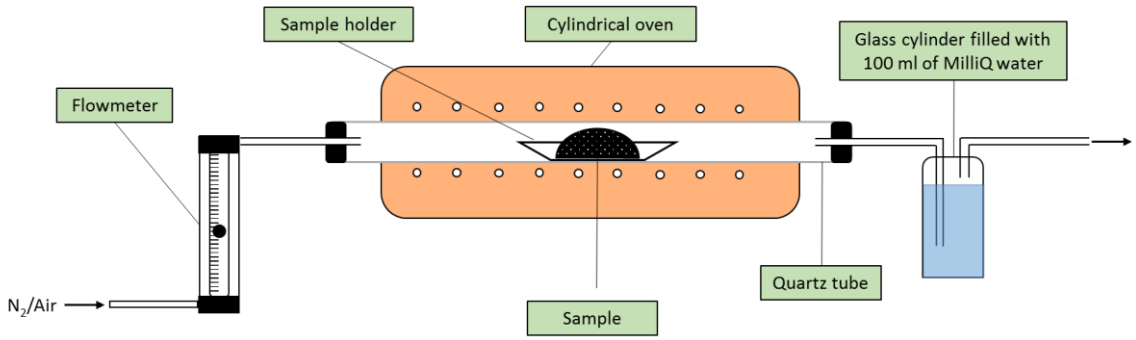

Figure 6: Set-up of the furnace.

3.2 Determination of metal concentrations in solid samples by ICP analysis

An iCAP™ 6000 Series ICP-OES was used to determine the metal concentrations in the electrodes before and after the thermal treatment. The samples were dissolved using aqua regia (Merck Millipore Nitric acid 65% - EMD Millipore Hydrochloric acid 37%) as the leaching agent, at approximately 80ºC and using magnetic stirring. After dissolution, the samples were filtered. The solid sample, remaining on the filter, was washed, dried and weighed. Qualitative information about this undissolved fraction was obtain using X-ray diffraction (XRD) analysis. The samples were diluted with a 0.5M HNO_3 solution.

3.3 X-Ray powder Diffraction qualitative analysis of crystalline compounds - XRD

The XRD analyses were carried out using a Siemens D5000 X-ray diffractometer, using an accelerator voltage of 40 kV and a current of 40 mA. The X-ray wavelength used corresponds to the characteristic Cu K-radiation, and a 2Θ range from 10° to 80° was included in the scans. Furthermore, sample rotation, with a rotation speed of 15 rpm, was used in order to avoid the effect of any preferential orientation of the crystals giving rise to incorrect peak heights.

The diffraction data obtained was evaluated by comparison with standard data for known compounds in the JCPDS database [36]. This method allows for the identification of crystalline compounds present in concentrations of ca. 2 weight%. Amorphous compounds cannot be identified.

3.4 Thermodynamic considerations

The HSC Chemistry 9 software, developed by Outotec, was used to carry out thermodynamic calculations, in order to propose a hypothesis about the reaction mechanisms that were involved during the thermal treatment. These theoretical results were then compared with the experimental results.

3.5 Fourier Transform Infrared Spectroscopy analysis of the gas produced during the thermal treatment - FTIR

The instrument used was a Perkin Elmer Spectrum Two FT-IR Spectrometer - Standard Detector, equipped with a LiTaO3 detector, which has a range between 15700 – 370 cm-1. The sample holder was a cell equipped with gas-tight taps, whose ends are closed with flat-glass KBr walls, transparent to IR. Since the gas density is low, the optical path is quite long, about 10 cm.

3.6 Analysis of carbon content based on combustion in O_2

A LECO CS744 instrument was used to determine the carbon content of the samples before and after pyrolysis.

3.7 Ion chromatography

The MilliQ water, used to wash the gas exiting from the furnace, was analysed using a Dionex DX100 Ion chromatograph in order to measure the concentration of anions. The column used was a Dionex IonPacTM AS4A-SC RFICTM 4x250 mm Analytical. The eluent was a solution of 1.7 mM $NaHCO_3$ and 1.8 mM Na_2CO_3. The pH of the washing water was also measured. The pH meter was calibrated using three buffer solutions at pH 1, 4, and 7 to an accuracy of ±0,02 pH units at 25°C (Radiometer Analytical SAS).

3.8 Balls mill for the mechanical removal of black mass from the aluminium layer

A Fritsch Planetary Mill Pulverisette 7 was used. The machine consists of a rotation plate with 2 symmetric holders. In each holder, it is possible to place a cylindrical ceramic sample holder with a lid containing 3 spherical balls with a diameter of 0.5 cm.

An equal number of cathodes and anodes were cut in to pieces with a size of a 2 cm^2. These pieces were then mixed homogeneously to prepare a set of samples.

The samples were placed in the furnace for 1.5 hours at 600 and 700°C. After the thermal treatment, the cathode and anode parts were again divided and separately inserted in the ball mill. The same treatment was applied to untreated samples to compare the efficiency of the black mass removal and contribution from the thermal treatment

4. Results and discussion

4.1 Characterization of the battery material

Starting with five LiB cells, the average weight of each cell was 553.1±0.2 g. The external plastic cover, 23.0 g ± 0.9, was removed. Internally, the battery cell consisted of 19 anodes interleaved with 18 cathodes. The weight of the black mass recovered from the cathode aluminium layers was approximately 218.2±0.8 g and represented the main component of the cell, followed by graphite (115.9±0.3 g), the copper foils (57.0±0.1 g), aluminium foils (36.0±0.1 g), and separators (42.2±0.5 g). A summary of this data can be seen in Figure 7.

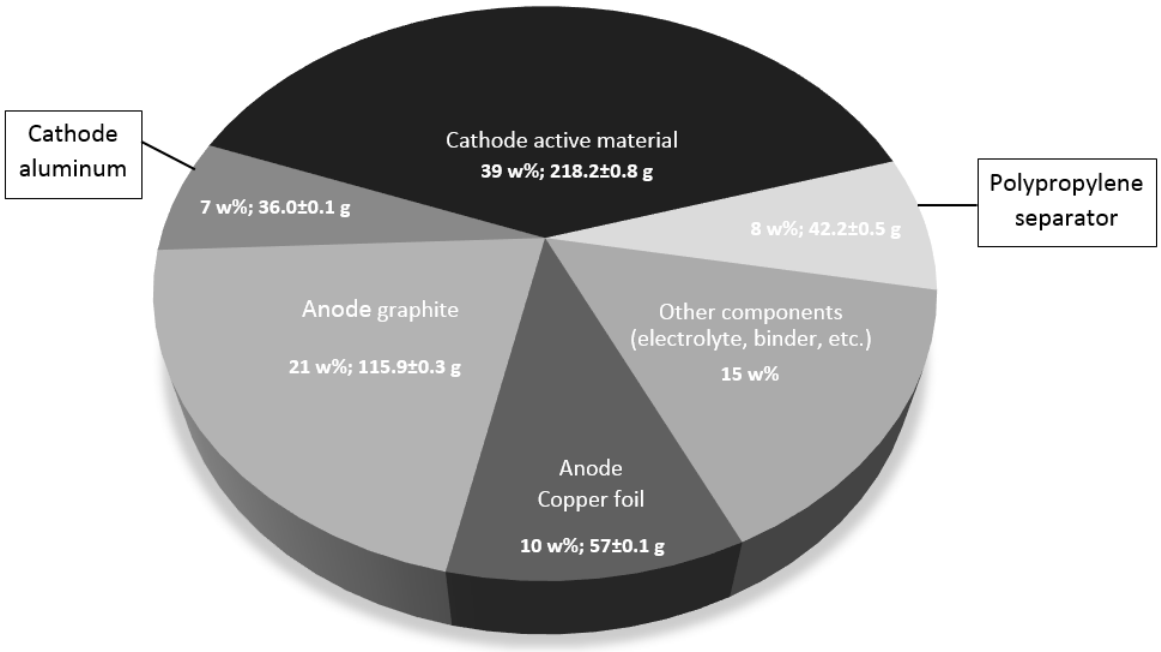

Figure 7: Mass balance of used material.

The composition and microstructure of samples consisting of a mixture of both of the electrodes were investigated. The concentrations of the metals in the battery, obtained by means of ICP-OES analysis, are given in Table 1.

Table 1: Metal composition of the battery [wt%]

Mn	Ni	Co	Cu	Li	Al
11.0±0.7	5.6±0.3	5.5±0.3	12.3±0.8	2.4±0.2	6.8±0.5

Analysing cathode and anode separately, it was observed, as expected, that the composition of the two types of electrodes was considerably different (Table 2): Cu was only detected in the anode; Al, Co, Mn and Ni in the cathode, whereas Li is present in both electrodes.

Table 2: Metal composition of the electrode material [wt%].

Element	Mn	Ni	Co	Cu	Li	Al
Anode	nd	nd	nd	27.2±0.8	0.1±0.2	0.00
Cathode	19.0±0.7	9.0±0.3	9.1±0.3	nd	3.7±0.2	10.3±1.2

nd = not detected

The XRD diffractogram of the solid fractions remaining after the attempted total dissolution of the samples is shown in Figure 8. It shows a hump at low angles. This is due to the amorphous nature of the polymers, i.e. the separator material, which is most commonly polypropylene and PVDF. When dissolving cathodes and anodes separately, it was confirmed that the undissolved fraction obtained from the negative electrodes is essentially graphite. The spectrum of the cathode shows the diffraction pattern produced by the separator material, polypropylene (PP). It was not possible to identify any diffraction from the PVDF because of its amorphous state. Diffractions originating from Al_2O_3 were also detected. This oxide is formed by the natural oxidation of the surface of the aluminium foil and it is particularly resistant to acid attack, even by aqua regia.

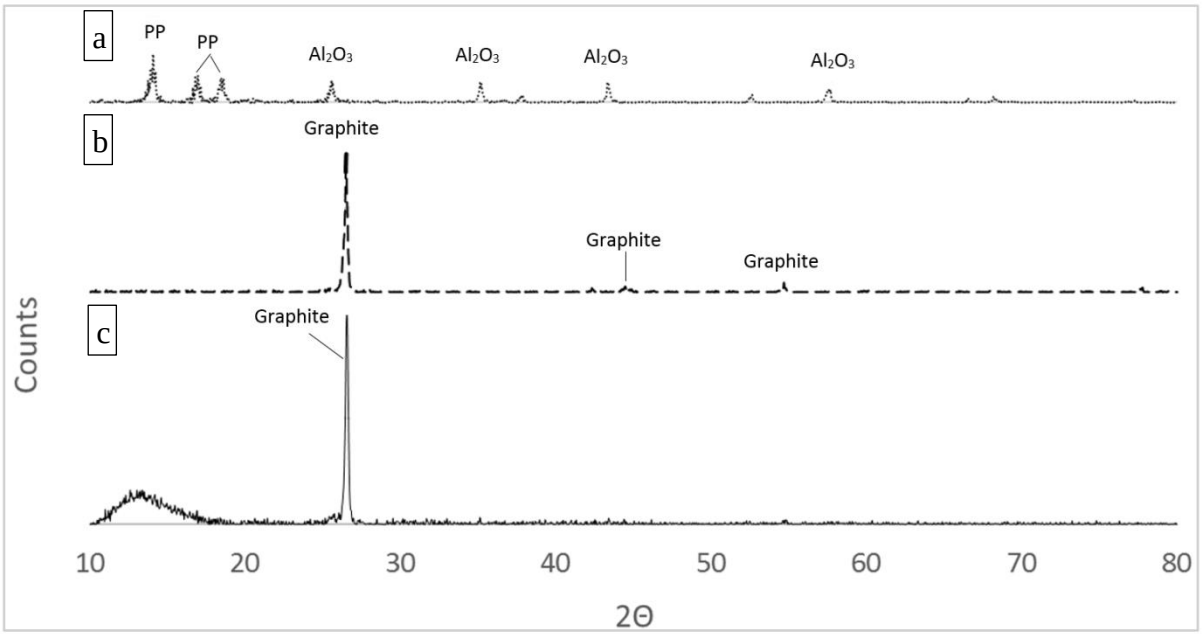

Figure 8: The XRD diffractogram of undissolved fraction (after aqua regia) (a) cathode material, (b) anode material, and (c) equal quantities of cathode and anode materials.

The microstructural study performed by XRD of samples consisting of a mixture of both electrodes identified the presence of Cu and Al, both in elemental form and oxide form as shown in Figure 9. The most intense peak at 27˚ is generated by the graphitic carbon.

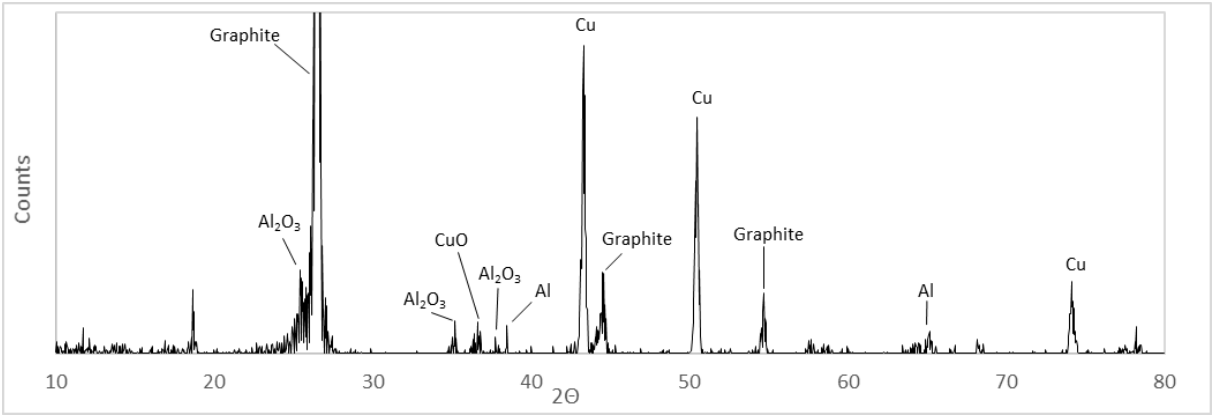

Figure 9: The XRD diffractogram of mixed electrode materials (anode and cathode).

The complexity and, in some cases, similarity of the spectra for transition metal oxides makes it difficult to identify the specific Co, Ni, and Mn oxides present. Therefore, further XRD analysis was performed on just the active cathode material, as shown in Figure 10, which was mechanically separated from the aluminium layer. The peak at 18.7˚ is common for all three

lithium-containing metal oxides that are expected to be present in the samples. Therefore, the absence of this peak in the diffractogram of the treated samples can be taken to confirm the complete decomposition of the lithium metal oxides in the treatment steps.

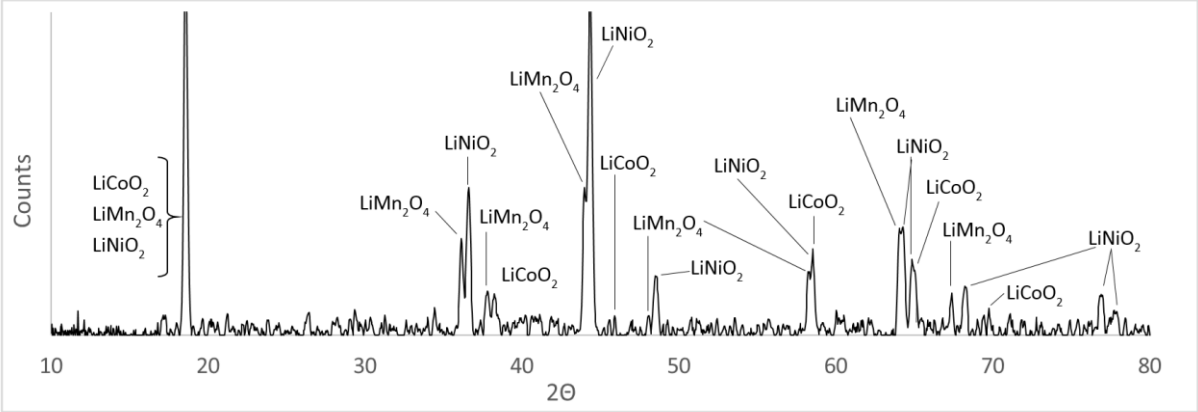

Figure 10: The XRD diffractogram of cathode material.

4.2 Thermodynamic considerations

The carbon present in the samples triggers a carbothermic reduction of metal oxides through the gaseous intermediate CO. The oxides were considered individually and their possible interactions with C and CO were studied theoretically at temperatures between 300 and 800˚C and standard pressure.

4.2.1 Pyrolysis

4.2.1.1 $LiCoO_2$

$LiCoO_2$ was shown to be stable at temperatures below 850˚C. At temperatures higher than 300˚C, C and CO can reduce this metal oxide: $Co^{(+3)}$ is reduced to Co(met) and $Co^{(+2)}O$ by means of reactions (1)-(5). $Li^{(+1)}$ is not reduced and form $Li_2{}^{(+1)}O$. The plot in Figure 11a shows how ΔG^0 varies with temperature for these reactions.

$$4LiCoO_2(s) + 3\,C(s) \rightarrow 2\,Li_2O(s) + 4\,Co(s) + 3\,CO_2(g) \quad (1)$$

$$4LiCoO_2(s) + C(s) \rightarrow 2Li_2O(s) + 4CoO(s) + CO_2(g) \quad (2)$$

$$2LiCoO_2(s) + 3C(s) \rightarrow Li_2O(s) + 2Co(s) + 3CO(g) \quad (3)$$

$$2LiCoO_2(s) + C(s) \rightarrow Li_2O + 2CoO(s) + CO(g) \quad (4)$$

$$2LiCoO_2(s) + 3\,CO(g) \rightarrow Li_2O(s) + 2Co(s) + 3CO_2(g) \quad (5)$$

An increase in temperature promotes the reactions of $LiCoO_2$ with C. On the other hand, the reaction of $LiCoO_2$ with CO, as described by reaction (5), is only slightly influenced by variation in temperature and it appears to be the most favourable at temperatures up to 700°C. Around this temperature, the three reactions become competitive, with $\Delta G^0 \approx$-128 kJ. Through the spontaneous reactions (6) and (7), CoO can react further with C and CO giving Co and CO_2 as products:

$$C(s) + 2CoO(s) \rightarrow 2Co(s) + CO_2(g) \quad (6)$$

$$CO(g) + CoO(s) \rightarrow Co(s) + CO_2(g) \quad (7)$$

To summarize: the results show that Li tends to maintain its oxidation state and form the stable Li_2O, whereas Co tends to be reduced from oxidation state +3 to +2 or even further to Co metal. Graphite is converted into CO and CO_2. The possible reaction between CO_2 and Li_2O gives Li_2CO_3 as product, as described by equation (8). This reaction has $\Delta_r G^0_T$ = 0.14T-174.58 (0-1000°C), thus, the slope is positive but the reaction is permitted thermodynamically because its ΔG^0 remains negative in the temperature range under consideration.

$$CO_2(g) + 2Li_2O(s) \rightarrow Li_2CO_3(s) \quad (8)$$

Thus, Co and Li_2CO_3 can be the main solid products of the carbothermic reduction. $LiCoO_2$ can react with C and CO and form Co, Li_2CO_3, and gases (CO and CO_2), by the following reactions:

$$2LiCoO_2(s) + 3CO(g) \rightarrow 2Co(s) + Li_2CO_3(s) + 2CO_2(g) \quad (9)$$

$$6LiCoO_2(s) + 5C(s) \rightarrow 6Co(s) + 3Li_2CO_3(s) + CO_2(g) + CO(g) \quad (10)$$

Based on the above considerations, reaction (10) is the most favourable thermodynamically and it is plotted in Figure 11b, as described by the equation $\Delta_r G^0_T$ =-0.58T-211.97(0-1000°C).

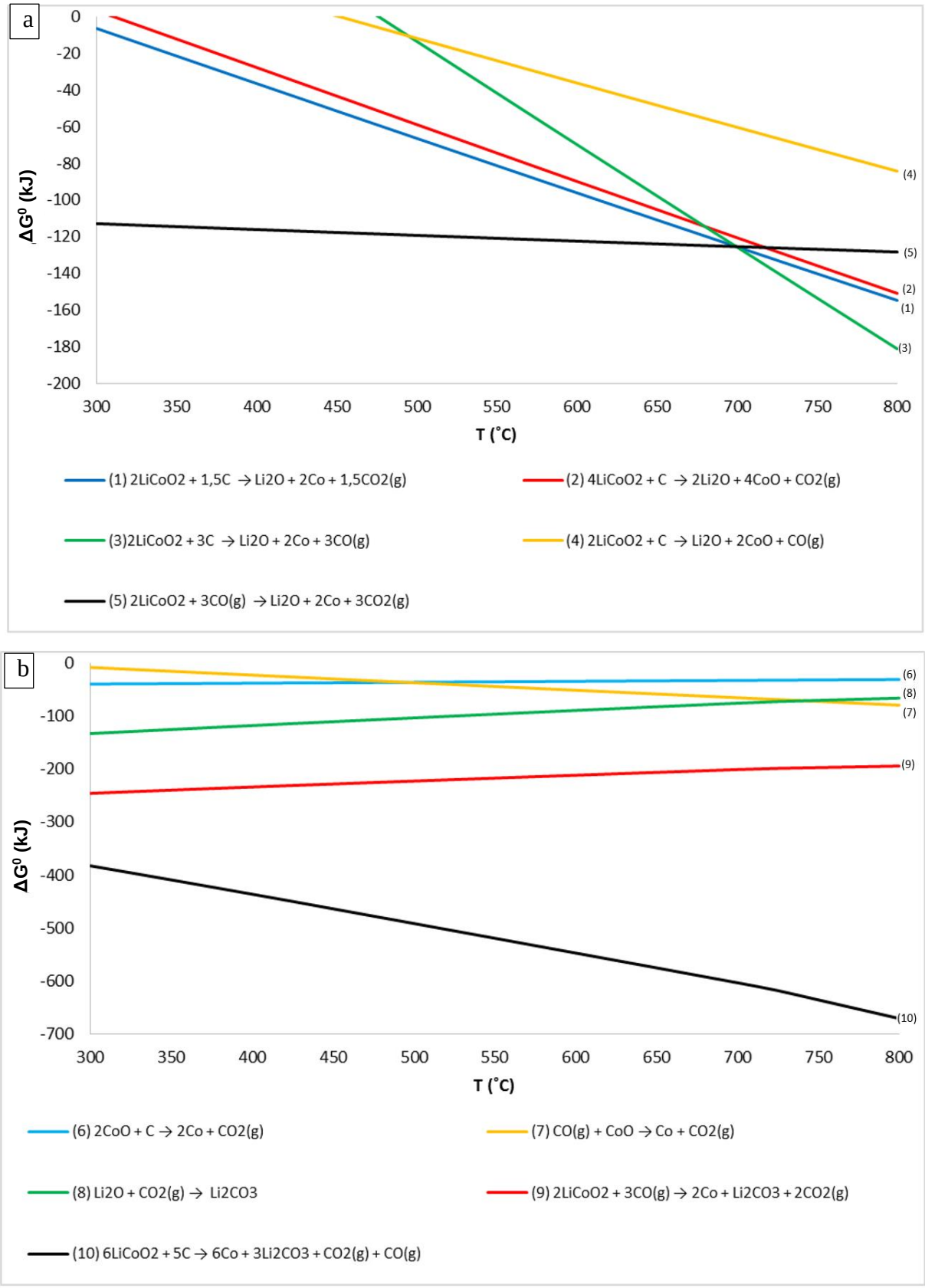

Figure 11a and b : Plots of ΔG^0 (kJ) vs T (°C) for the reduction of $LiCoO_2$ and by-products with C or CO.

4.2.1.2 $LiMn_2O_4$

Thermodynamic data regarding $LiMn_2O_4$ was not available in the HSC 9 database. Therefore, a separate database was created using the entropy and heat capacity data published by Knyazev [41] and enthalpy data published by Lai [42]. These extensions of the database permitted the extrapolation of ΔG^0 up to 126.85 °C. Above that temperature, the thermodynamic parameters were correlated using the same software.

The calculation results show that $LiMn_2O_4$ should not spontaneously decompose in the chosen range of temperature. The reactions with C or CO give Mn_3O_4, Li_2CO_3, and Li_2O as products, as described by (11) and (12). Mn with oxidation states +3 and +4 in $LiMn_2O_4$ are reduced to Mn with oxidation states +2 and +3 in Mn_3O_4. The thermodynamic plots of ΔG^0 versus T for these reactions are shown in Figure 12. Mn with oxidation states +3 and +4 can also be reduced by C to give $Mn^{(+2)}O$ and CO as products, as described by reaction (13). This reaction has a more negative slope for the curve describing the dependence of Gibbs free energy on T, compared to those of reactions (9) and (10). This curve can be described by the equation $\Delta_r G^0_T = -0.227T-138.62$. $Li^{(+1)}$ is not reduced and forms the Li_2CO_3.

$$2.4LiMn_2O_4(s) + C(s) \rightarrow 1.2Li_2O(s) + 1.6Mn_3O_4(s) + CO_2(g) \quad (11)$$

$$3LiMn_2O_4(s) + 2.5CO(g) \rightarrow 2Mn_3O_4(s) + 1.5Li_2CO_3(s) + CO_2(g) \quad (12)$$

$$2LiMn_2O_4(s) + 2C(s) \rightarrow Li_2CO_3(s) + 4MnO(s) + CO(g) \quad (13)$$

Theoretically, MnO could be oxidized to Mn_3O_4 by the reaction with $LiMn_2O_4$, as described by (14). However, this oxidation is not thermodynamically permitted, because the Gibbs free energy is positive in all of the temperature range under consideration. Instead, MnO can act as a reducing agent in the carbothermic reaction of $LiMn_2O_4$, as shown in (15) and (16). The thermodynamic calculations show that the reaction (16) of $LiMn_2O_4$ with CO, in the presence of MnO, has a ΔG^0 lower throughout all of the temperature range compared to the one without MnO, reaction (12).

$$2LiMn_2O_4(s) + 5MnO(s) \rightarrow Li_2O(s) + 3Mn_3O_4(s) \quad (14)$$

$$2.8LiMn_2O_4(s) + MnO(s) + C(s) \rightarrow 1.4Li_2O(s) + 2.2Mn_3O_4(s) + CO_2(g) \quad (15)$$

$$4LiMn_2O_4(s) + MnO(s) + 3CO(g) \rightarrow 2Li_2CO_3(s) + 3Mn_3O_4(s) + CO_2(g) \quad (16)$$

This means that MnO can be involved in the reduction of the $Mn^{(+3)(+4)}$ but C and CO would be the main reductants agents.

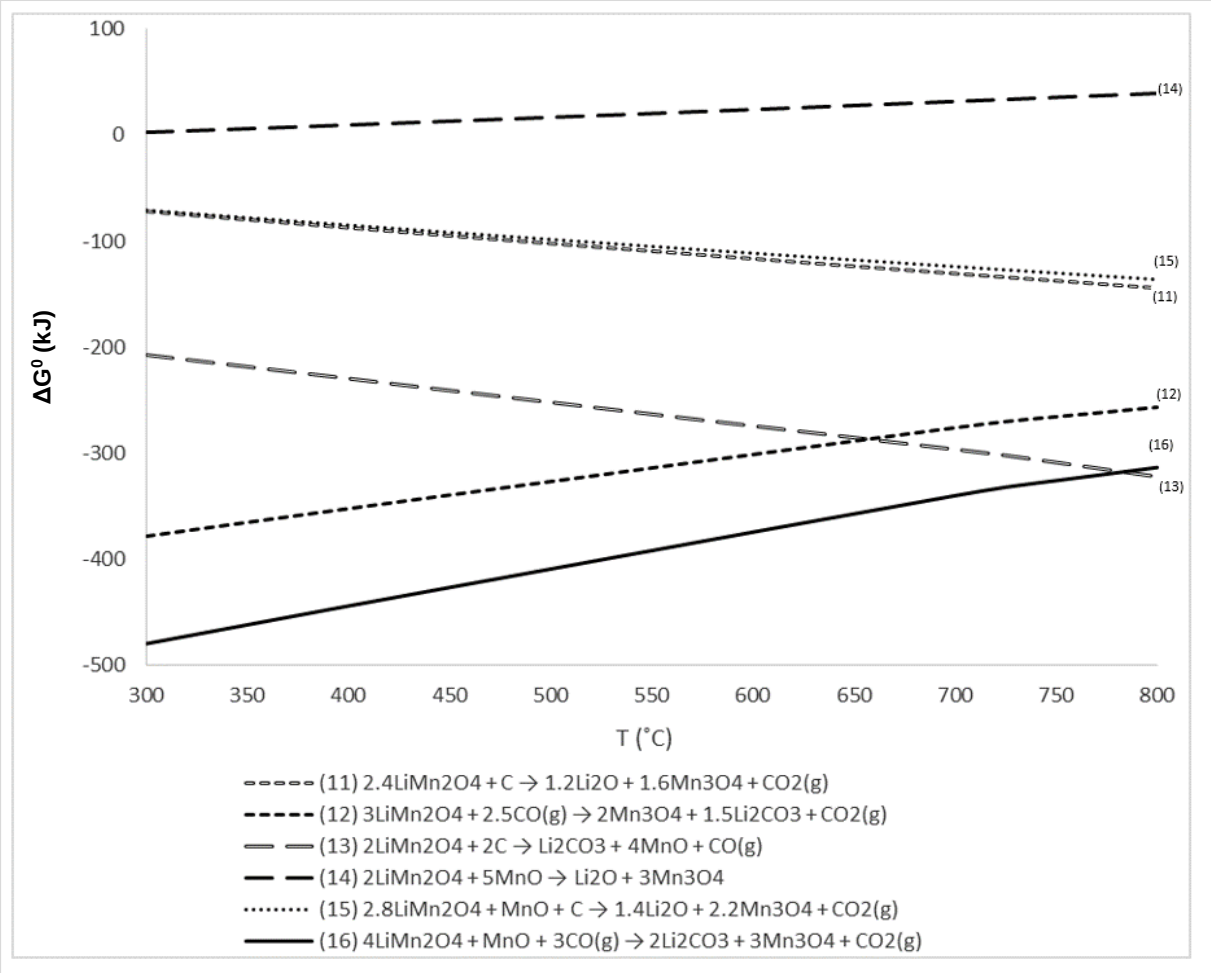

Figure 12: Plot of ΔG^0 (kJ) vs T (°C) for the most thermodynamically favoured reactions for the decomposition of $LiMn_2O_4$.

4.2.1.3 $LiNiO_2$

There is not enough data in the HSC Chemistry database available for $LiNiO_2$ but its behaviour was modelled as being similar to that of $LiCoO_2$.

The carbothermic reduction of $Ni^{(+3)}$ can give $Ni(^0)$ and $Ni^{(+2)}O$ as the main products. The $Ni^{(+2)}O$ can, in its turn, be reduced by C and CO into $Ni^{(0)}$ with the associated formation of CO_2, as described by reactions (18) and (19). The corresponding plot of ΔG^0 as a function of T is shown in Figure 13.

$$4LiNiO_2(s) + C(s) \rightarrow 2Li_2O(s) + 4NiO(s) + CO_2(g) \quad (17)$$

$$2LiNiO_2(s) + 3C(s) \rightarrow Li_2O(s) + 2Ni(s) + 3CO(g) \quad (18)$$

$$2LiNiO_2(s) + C(s) \rightarrow Li_2O(s) + 2NiO(s) + CO(g) \quad (19)$$

$$2LiNiO_2(s) + 3CO(g) \rightarrow 2Ni(s) + Li_2CO_3(s) + 2CO_2(g) \quad (20)$$

$$6LiNiO_2(s) + 5C(s) \rightarrow 6Ni(s) + 3Li_2CO_3(s) + CO_2(g) + CO(g) \quad (21)$$

$$C(s) + 2NiO(s) \rightarrow 2Ni(s) + CO_2(g) \quad (22)$$

$$CO(g) + NiO(s) \rightarrow Ni(s) + CO_2(g) \quad (23)$$

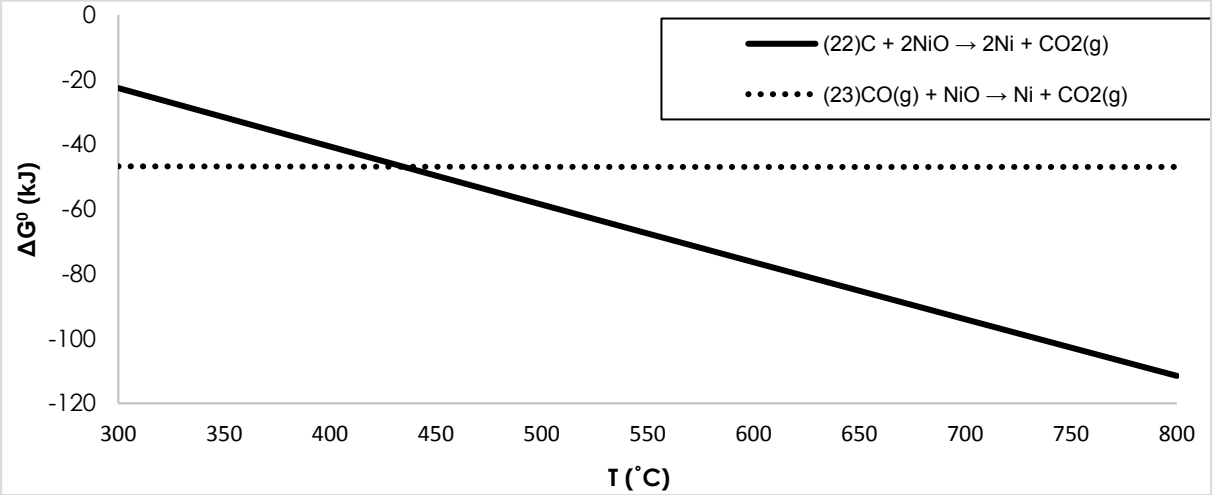

Figure 13: Plot of ΔG^0 (kJ) vs T (°C) for the carbothermic reduction of NiO.

4.2.2 Incineration

The high temperature induces combustion of the graphite and the organic materials with the formation of CO_2 and CO, reactions (24), (25), (26), as shown in Figure 14.

$$C(s) + O_2(g) \rightarrow CO_2(g) \quad (24)$$

$$2C(s) + O_2(g) \rightarrow 2CO(g) \quad (25)$$

$$2CO(g) + O_2(g) \rightarrow 2CO_2(g) \quad (26)$$

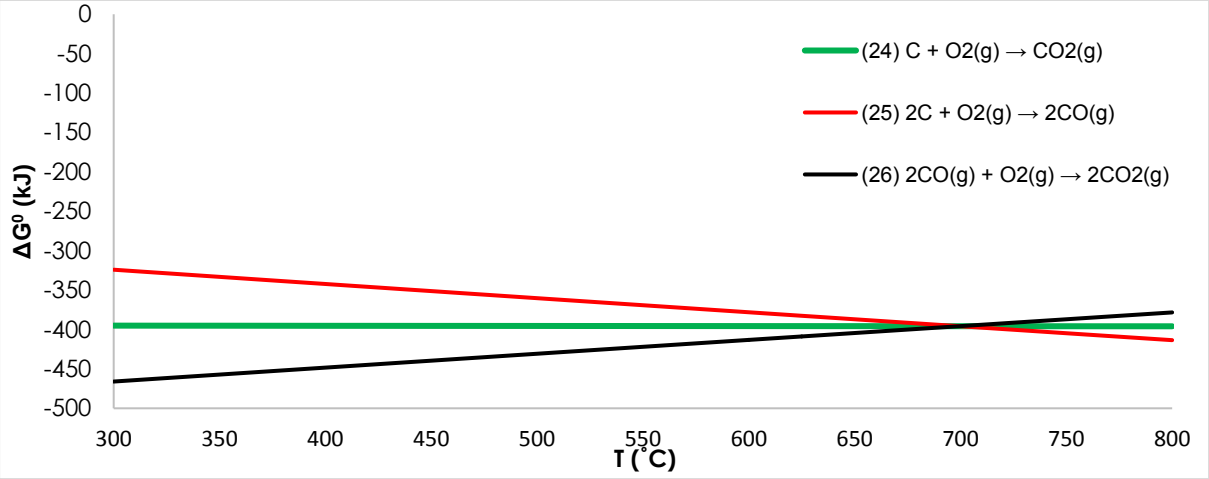

Figure 14: Plot of ΔG^0 (kJ/mol) vs T (°C) for the reaction of C and CO with O_2.

CO_2 is the thermodynamically most favoured product at temperatures below 700°C. It was expected that the C in the samples would not be completely consumed by the incineration and that its abundance was sufficient to provide the carbothermic reduction of the metal oxides. The thermodynamic calculations for the reduction of the metal oxides were carried out separately for each metal. Their interaction with C, CO and O_2 was studied in the temperature range 300 to 800˚C at standard pressure.

4.2.2.1 $LiCoO_2$

C and CO reduce the $Co^{(+3)}$ present in the $LiCoO_2$ in the formation of $Co^{(+2)(+3)}{}_3O_4$, in the presence of O_2, as described in reactions (27) and (28). Li_2CO_3, and CO_2 are the other products of these reactions. The $Co_3{}^{(+2)(+3)}O_4$ is further reduced to $Co^{(+2)}O$ and $Co^{(0)}$, according to the reactions (29)-(32). The trends for ΔG^0 dependence on T for these reactions are shown in Figure 15.

$$3LiCoO_2(s) + 2.5C(s) + 2.25O_2(g) \rightarrow Co_3O_4 + 1.5Li_2CO_3(s) + CO_2(g) \quad (27)$$

$$3LiCoO_2(s) + 2.5CO(g) + O_2(g) \rightarrow Co_3O_4(s) + 1.5Li_2CO_3(s) + CO_2(g) \quad (28)$$

$$Co_3O_4(s) + 2C(s) + O_2(g) \rightarrow 3CoO(s) + CO(g) + CO_2(g) \quad (29)$$

$$3Co_3O_4(s) + 5CO(g) + O_2(g) \rightarrow 9CoO(s) + 5CO_2(g) \quad (30)$$

$$1.6CoO(s) + 1.8C(s) + O_2(g) \rightarrow 1.6Co(s) + 1.8CO_2(g) \quad (31)$$

$$7CoO(s) + 9CO(g) + O_2(g) \rightarrow 7Co(s) + 7CO_2(g) \quad (32)$$

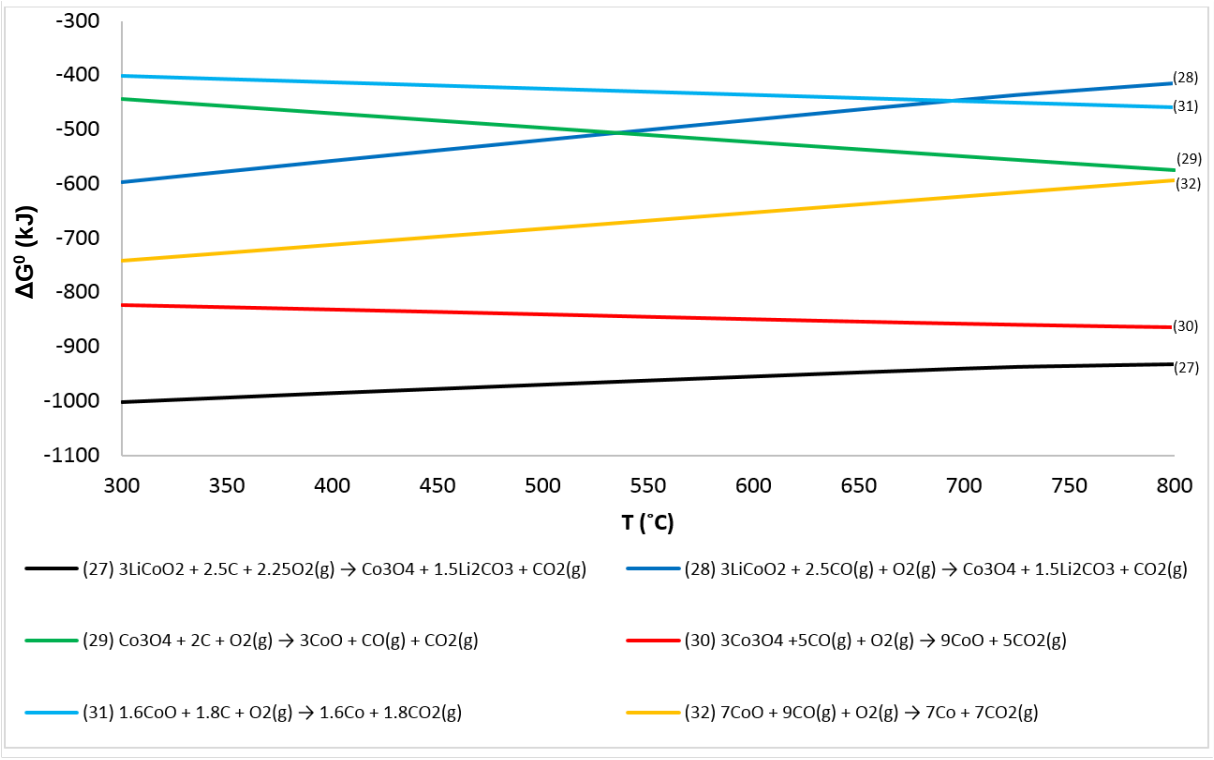

Figure 15: Plot of ΔG^0 (kJ) vs T (°C) for the reduction of $LiCoO_2$ with C.

4.2.2.2 $LiMn_2O_4$

$LiMn_2O_4$ is thermodynamically stable in the chosen temperature range. During the thermal treatment, the thermodynamics promotes the $Mn^{(+3)(+4)}$ reduction to $Mn^{(+2)(+3)}{}_3O_4$ and decomposition to $Mn^{(+4)}O_2$, as shown in the reactions (33), (34), (35), and (36). It can be expected that $Mn^{(+4)}O_2$ will react with C, CO and O_2 forming $Mn^{(+2)(+3)}{}_3O_4$ and $Mn^{(+2)}O$ as described in the reactions (37)-(40). $Li^{(+1)}$ can be present in the form of $Li^{(+1)}{}_2O$ and react with CO_2, forming $Li^{(+1)}{}_2CO_3$ according to reactions (41) and (42). These results are shown graphically in Figure 16.

$3LiMn_2O_4(s) + 7/3\ C(s) + O_2(g) \rightarrow 2Mn_3O_4(s) + 3/2Li_2O(s) + 7/3CO_2(g)$ (33)

$6LiMn_2O_4(s) + 5CO(g) \rightarrow 4Mn_3O_4(s) + 3Li_2O(s) + 5CO_2(g)$ (34)

$2LiMn_2O_4(s) + C(s) + 1.5O_2(g) \rightarrow 4MnO_2(s) + Li_2O(s) + CO_2(g)$ (35)

$2LiMn_2O_4(s) + CO(g) + O_2(g) \rightarrow 4MnO_2(s) + Li_2O(s) + CO_2(g)$ (36)

$1.6MnO_2(s) + 1.8C(s) + O_2(g) \rightarrow 1.6MnO(s) + 1.8CO_2(g)$ (37)

$MnO_2(s) + CO(g) \rightarrow MnO(s) + CO_2(g)$ (38)

$3MnO_2(s) + O_2(g) + 2C(s) \rightarrow Mn_3O_4(s) + 2CO_2(g)$ (39)

$3MnO_2(s) + 2CO(g) \rightarrow Mn_3O_4(s) + 2CO_2(g)$ (40)

$Li_2O(s) + CO_2(g) \rightarrow Li_2CO_3(s)$ (41)

$2Li_2O(s) + 2CO(g) + O_2(g) \rightarrow 2Li_2CO_3(s)$ (42)

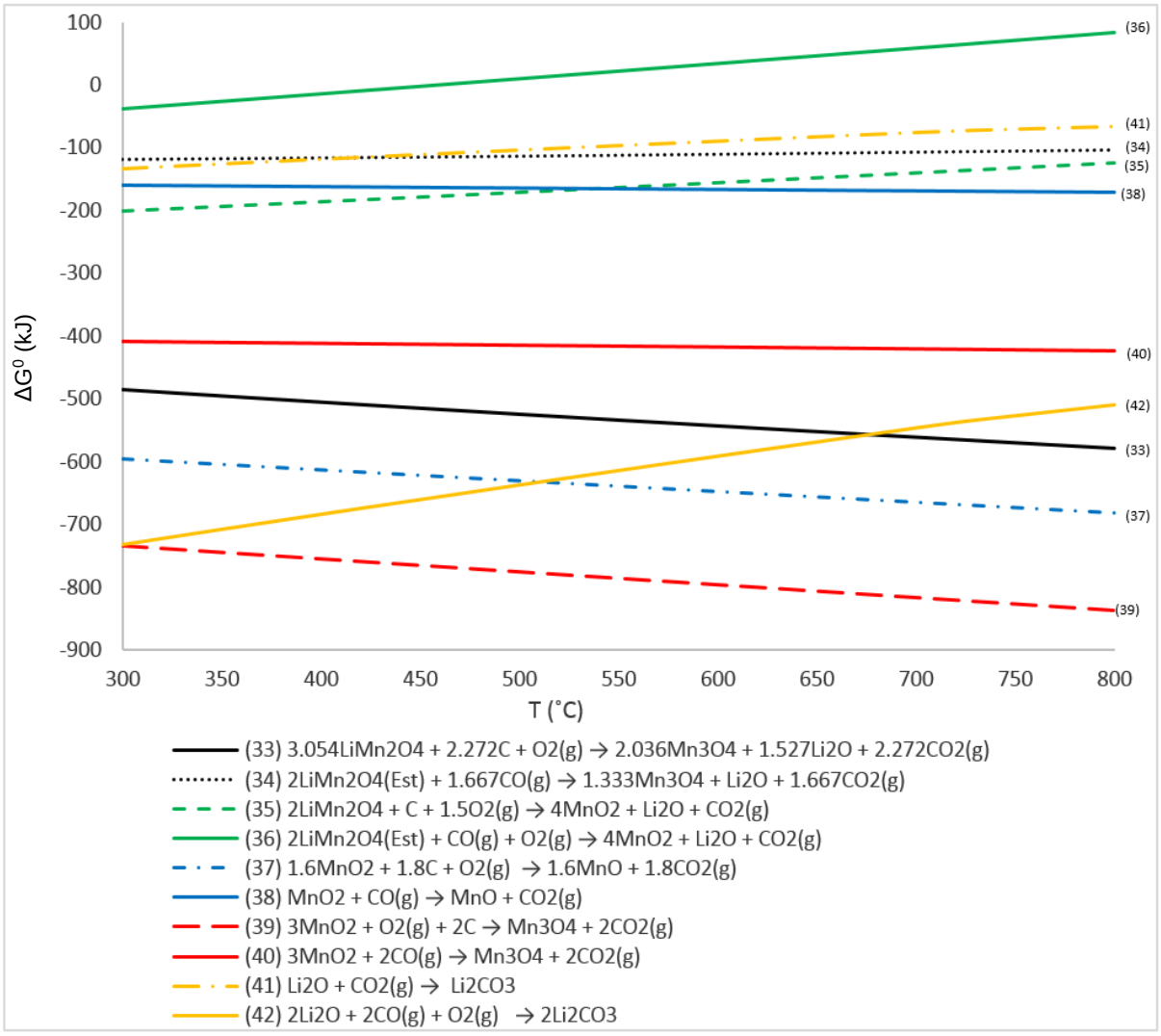

Figure 16: Plot of ΔG^0 (kJ) vs T (°C) for the reduction of $LiMn_2O_4$.

4.2.2.3 $LiNiO_2$

The reaction of $LiNiO_2$ with C and CO in presence of O_2 can give $Ni^{(+2)(+3)}{}_3O_4$ and Li_2CO_3 as the main products, according to reaction (43). $Ni^{(+2)(+3)}{}_3O_4$ can be further reduced by C and CO into Ni(met) and $Ni^{(+2)}O$, as described by reactions (44)-(46).

$$3LiNiO_2(s) + 2.5C(s) + 2.25O_2(g) \rightarrow Ni_3O_4(s) + 1.5Li_2CO_3(s) + CO_2(g) \quad (43)$$

$$Ni_3O_4(s) + 2C(s) + O_2(g) \rightarrow 3NiO(s) + CO(g) + CO_2(g) \quad (44)$$

$$1.6NiO(s) + 1.8C(s) + O_2(g) \rightarrow 1.6Ni(s) + 1.8CO_2(g) \quad (45)$$

$$7\ NiO(s) + 9\ CO(g) + O_2(g) \rightarrow 7\ Ni(s) + 9\ CO_2(g) \quad (46)$$

4.2.2.4 Carbonyl formation

According to the Boudouard reaction, the formation of CO starts at around 400°C and became the dominant for the formation of CO_2 at around 700°C. At this temperature, the atmosphere on the samples is reach of CO, and in this condition, it is possible that locally there is the formation of metal carbonyls, stable in a CO atmosphere according to the reactions (47)- (52). The trends for ΔG^0 dependence on T for the reactions that have Co, Mn and Ni carbonyls as products are shown in Figure 17.

$$2Co(s) + 8C(s) + 4O_2(g) \rightarrow Co_2(CO)_8(s) \quad (47)$$

$$2CoO(s) + 8C(s) + 3O_2(g) \rightarrow Co_2(CO)_8(s) \quad (48)$$

$$Mn_3O_4(s) + 15C(s) + 5{,}5O_2(g) \rightarrow 1{,}5Mn_2(CO)_{10}(g) \quad (49)$$

$$2MnO(s) + 10C(s) + 4O_2(g) \rightarrow Mn2(CO)10(g) \quad (50)$$

$$Ni(s) + 4C(s) + 2O_2(g) \rightarrow Ni(CO)_4(s) \quad (51)$$

$$NiO(s) + 4C(s) + 1{,}5O_2(g) \rightarrow Ni(CO)_4(s) \quad (52)$$

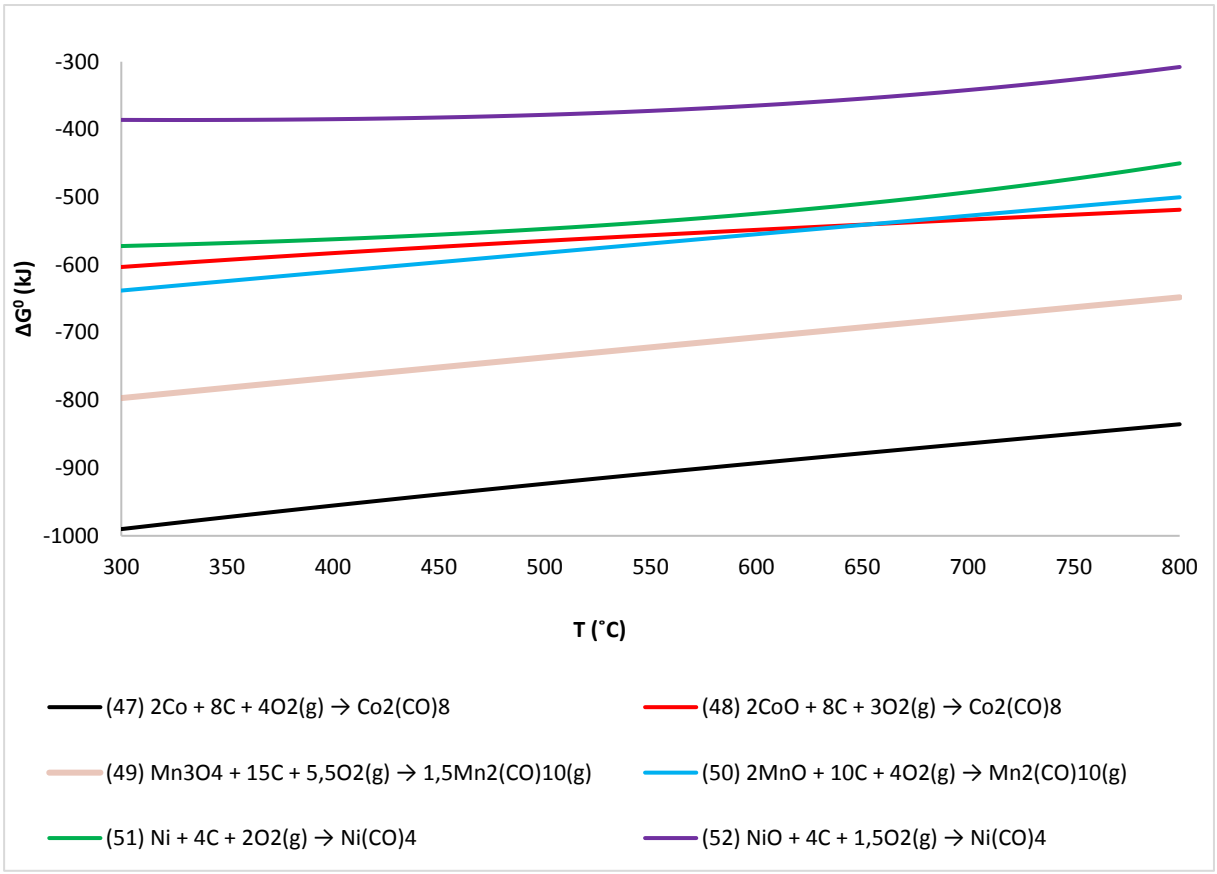

Figure 17: Plot of ΔG^0 (kJ) vs T (°C) for the reaction of formation of metal carbonyls,

4.3 Variation of weight during the thermal treatment

By measuring the weight of the samples before and after the thermal treatment, a general loss of mass was detected, which increases with the rise in temperature and the duration of the thermal treatment. Furthermore, all of the samples lost a significant part of their weight in the first 30 minutes of treatment, independent of temperature. This can be explained by the evaporation of the organic solvents present in the battery.

For the pyrolysis, only taking the rise in the temperature into consideration, ~22% of the weight of the samples (Δw%) treated at 700ºC was lost during 90 minutes of treatment, which is twice the weight loss obtained at 400 ºC, which can be observed in Figure 18a. On the other hand, the temperature increase from 500 to 600ºC did not have a noticeable effect on the sample weight. Considering the variation in the treatment time, Δw% is more evident at 700ºC than at lower temperatures. It varies from ~11% at 30 minutes to ~15.5 at 60 minutes and ~22% after 90

minutes. Overall, the Δw% obtained treating the battery cells for 90 minutes at 400 ºC is equal to the one obtained at 700ºC in just 30 minutes.

The Δw% is more consistent during incineration than during pyrolysis. At 400ºC and 500ºC, the decrease in weight from 30 and 90 minutes was almost proportional to the increase in the treatment time, this can be observed in Figure 18b. After 90 minutes, a loss of ~16% and 23% of the initial weight was noted for the samples respectively. On the other hand, the weight of the sample did not change significantly during heating at 600 or 700ºC for 60 or 90 minutes. The weight change is ~27% and ~35% at the respective temperatures and did not change when the length of incineration was increased. This result might be due to the complete removal of the C content during the first 30 minutes at 700 ºC and 60 minutes at 600 ºC.

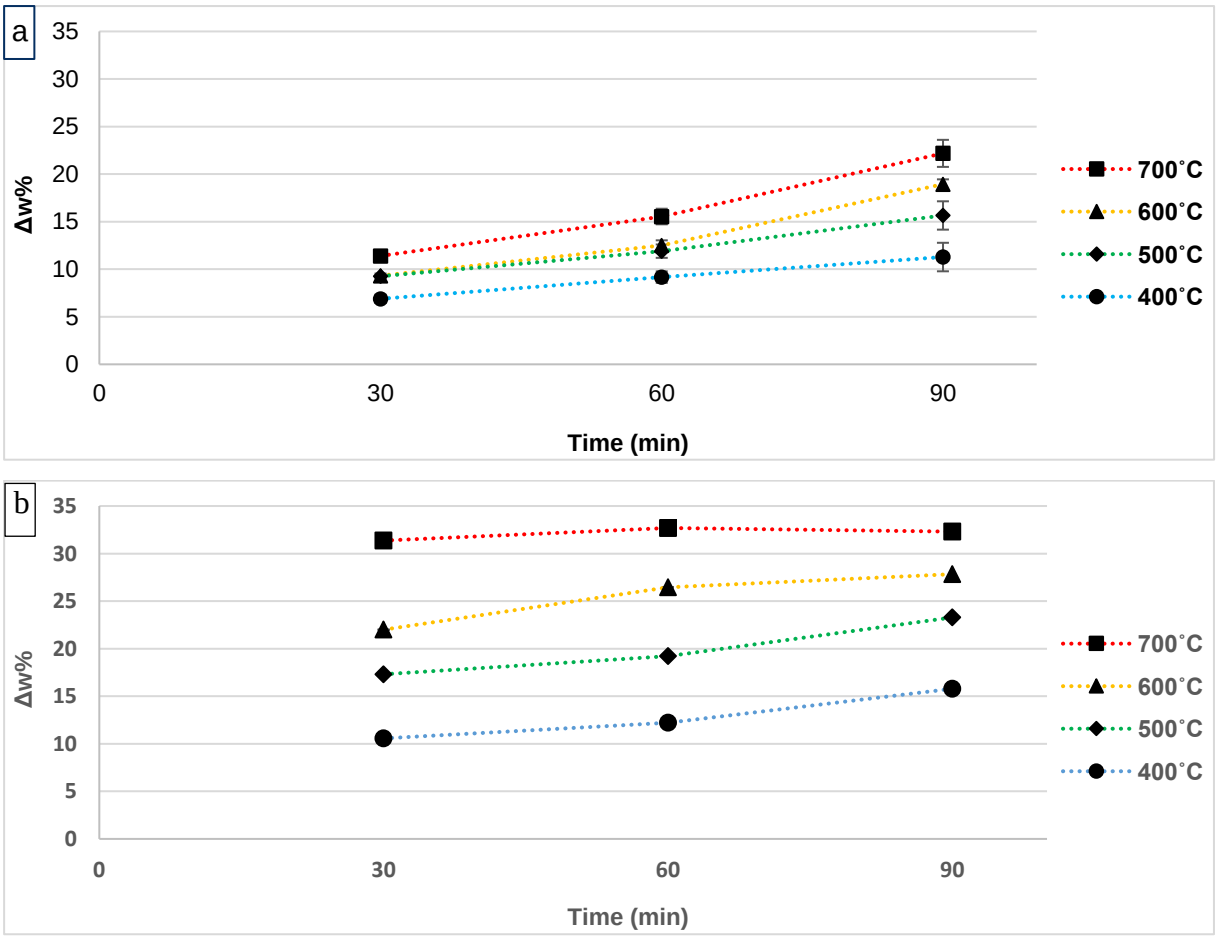

Figure 18: The dependence of the weight loss on the temperature and reaction time (a) pyrolysis; (b) combustion. The point (0;0) corresponds to the untreated material.

4.4 FTIR analysis of the gas produced during the thermal treatment

It follows from the thermodynamic considerations that one of the main products of pyrolysis should be carbon dioxide. To confirm this, analysis of the off-gas was performed using FTIR, as shown in Figure 19. The gas samples were collected 5 minutes after the start of treatment.

The FTIR spectra of the gases produced during pyrolysis and incineration show the same peaks. The peaks for CO_2 at 2400 cm^{-1} and between 3750 and 3600 cm^{-1} and the double peaks of CO around 2125 cm^{-1} are intense. This shows that the atmosphere in the system becomes rich in CO and CO_2. During pyrolysis, this is caused by the carbothermic reduction, accelerated by the high temperature, which involves the organic components and graphite in the battery. During incineration, this is also due to the action of the O_2 present in the air flow across the graphite and the organic compounds in the black mass. Comparing the two spectra in Figure 19, the quantity of CO_2 detected during combustion is higher than that obtained during pyrolysis. The symmetric peaks at 1400-1800 and 3550 -3900 cm^{-1} are typical of H_2O present as humidity in the system. The high temperature should promote degradation of the PVDF, which typically occurs through a mechanism of dehydrofluorination, as shown by reaction (53).

$$-(CH_2-CF_2-CH_2-CF_2)- \rightarrow -(CH_2-\underset{F}{CF}-\underset{H}{CH}-CF_2)- \rightarrow -(CH_2-CF=CH-CF_2)- + HF \quad (53)$$

It was expected that the presence of HF would be detected in the gas phase in the FTIR spectra. However, the signal for H_2O at high frequency probably obscures the signal for this acid. Evidence that the degradation of the binder takes place during combustion was obtained by analysing the MilliQ water, used to wash the gas leaving the furnace, for the presence of fluoride ions. The analysis did not show any significant difference in the amount of gaseous fluorides created when samples were treated at different times and temperatures. The average concentration of fluoride in the absorption solutions was 2.3±0.1 mM, and the average pH value of these solutions was 3.0± 0.3, for pyrolysis, and 2.7±0.1 mM and 3.1± 0.3 for incineration. Neither the Ion Chromatography nor FTIR performed on the absorption liquid showed any presence of volatile phosphates, which could be expected due to the decomposition of the electrolyte.

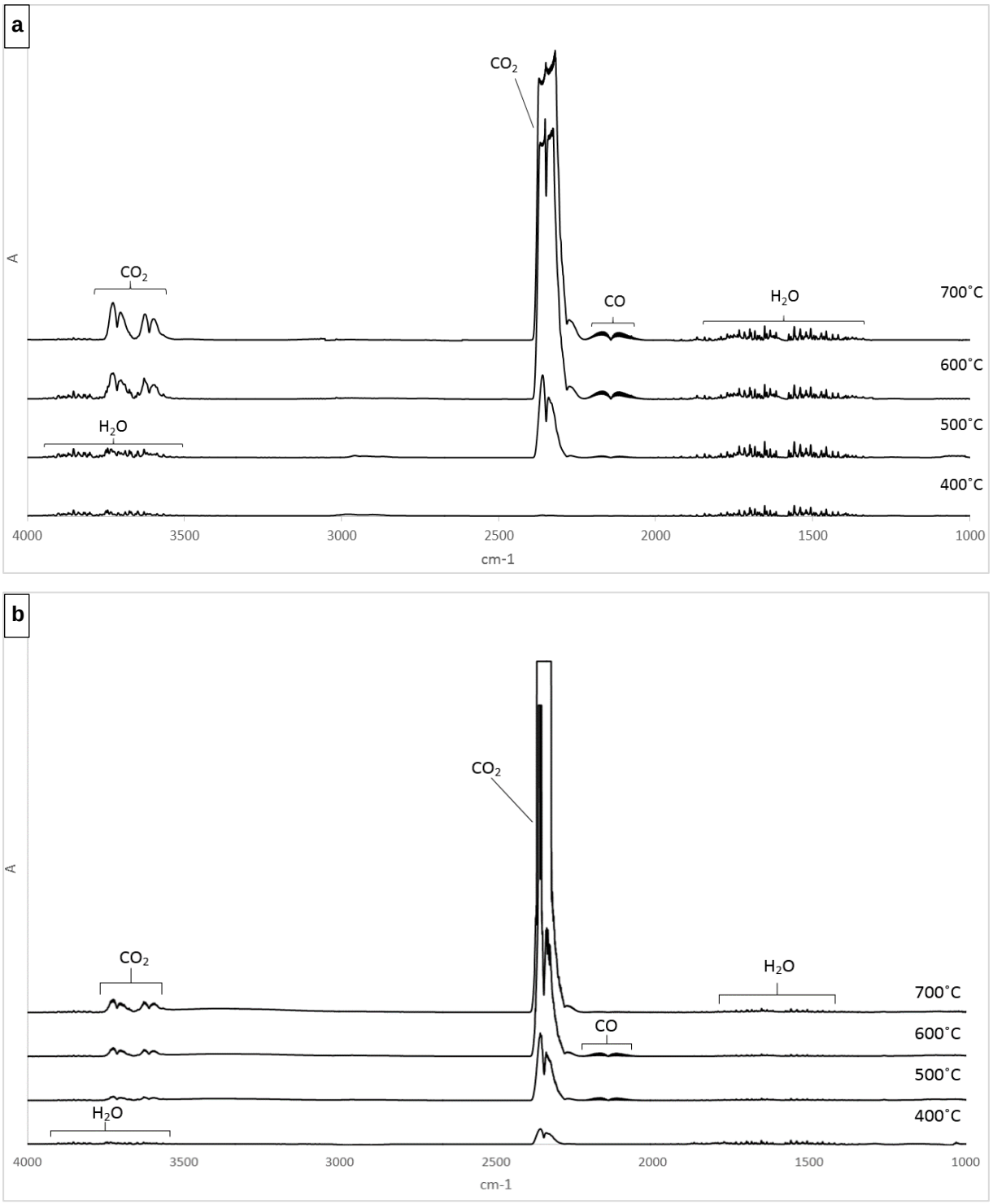

Figure 19: Comparison of absorbance spectra for samples treated for 5 minutes at 400˚, 500˚, 600˚, and 700°C. (a) for pyrolysis; (b) for combustion.

4.5 Organic by-product of the thermal treatment

During the treatment, the high temperature leads to the decomposition of the organic substances that are present in the samples. These substances evaporate inside the furnace and are transported to the end section of the quartz tube by the constant gas flow. This section of the quartz tube is outside the furnace and is colder, here the organic substances condense, covering the internal part of the tube, which can be observed in Figure 20.

This organic by-product has a brown- yellow colour and a density similar to an oil. It is probably a mixture of many decomposition products; therefore, the identification of its exact composition is complex. However, it was observed that this oil consists of a less polar fraction, soluble in petroleum ether (Fraction 1), and a more polar one (Fraction 2), soluble in acetone. Therefore, the oil was collected by firstly washing the tube with acetone, then with water and ether.

To collect the Fraction 1, petroleum ether was added to a part of the oil to dissolve the less polar fraction in it. This solution was then filtered leaving it to filter for gravity through a glass Pasteur pipette with an inner lining of cotton as a filtering material. To collect the Fraction 2 was used the same procedure dissolving a part of the oil in acetone and then filtering it.

An oil sample and a sample of each of the two fractions collected were sent to the Medac LTD laboratory to determine the carbon, hydrogen, and fluorine content.

Figure 20: The internal section of the quartz tube covered with the organic by-product.

Table 3: The elemental analysis of carbon, hydrogen, and fluorine performed by Medac LTD. Accuracy is ±0.30% absolute.

	Element (w%)		
	C	H	F
Oil	48.72	6.60	7.07
Fraction 1 (non-polar)	85.19	14.02	0.91
Fraction 2 (polar)	45.15	5.64	35.04

As can be seen from Table 3, the oil is mainly composed of carbon and hydrogen. A small quantity of fluorine was identified. Fraction 1 is almost totally composed of C and H, dividing the percentage of C and H by their respective atomic mass, it can be seen that the ratio of carbon and hydrogen is 1:2. It can therefore be assumed that Fraction 1 most probably consists of molecules containing chains of $-CH_2-$ produced by the decomposition of the polypropylene separator. In Fraction 2, instead, the amount of fluorine represents one third of the total (35.04%). This indicates that the most polar fraction formed was mainly composed of decomposition products from the PVDF. Therefore, fluorine was not removed completely from the system by the gas flow, as hydrofluoric acid, but remained partially in this organic by-product.

4.6 The influence of the thermal treatment on the concentration of metals in the black mass samples

It was possible to confirm that the weight variation in the samples was mainly caused by consumption of the graphite and the organic substances during heating, with the formation of volatile species. Such removal of organic components increases the purity of the metal-bearing material. The ICP-OES data, in Table 4 and 5, show a general increase in the concentration of metals in the sample with increasing temperature and length of treatment. It was expected that the Al (melting point 660˚C) would melt in the samples treated at 700˚C, thus coating the black mass. Instead, comparing an untreated cathode with one treated at 700˚C for 90 minutes, in

Figure 21, no evidence of Al melting was observed. The sample treated at 700 ˚C showed almost the same metal concentrations as the sample treated at 600 ˚C. No change in the rectangular shape of the cathode, or presence of melted aluminium on its surface, was observed. The presence of Al_2O_3 on the surface of the Al layer, having a higher melting point and low thermal conductivity, slows down the melting. The remaining black mass was easily separated from the metal foil due to the fact that the binder had decomposed.

Figure 21: Comparison of an untreated cathode (left) with one treated at 700˚C for 90 minutes (right).

Decomposition of the $LiPF_6$, with the formation of $PF_{5(g)}$, and so an evident decrease in the P concentration in the samples was expected. The decomposition temperature of $LiPF_6$ is ~215°C. Instead, the concentration of phosphorous increased for the metals investigated. This indicates that this salt had not been fully decomposed.

4.6.1 Pyrolysis

As shown in Table 4, Al and Cu, both from the metal foils, and Mn were the most abundant metals in the black mass (>10 w%), followed by Co and Ni (~7 w%). Li had an abundance of around 3 w%. As expected, the rise in the metal concentrations during heat treatment is almost proportional to the decrease in the weight of the sample. In the samples treated at 700˚C for 1.5 h, indeed, the weight loss equalling ~22% corresponded to an increase in metals w% of approximately ~25%. Al is an exception, since its concentration rises by almost 50%. This is due to the possible reduction of Al_2O_3 to Al during pyrolysis in the complex pyrolysis environment. The Al_2O_3 present in the untreated samples, is not dissolved by aqua regia and its presence was detected in the undissolved fraction. This affects the accuracy of the determination of the real Al concentration in samples.

The data in both Table 4 and Figure 18a show that the weight of the samples treated at 500 and 600˚C does not differ significantly. This can be explained by the fact that the decomposition of the organic material present in the battery occurs already at 400˚C. Indeed, a TGA study of PVDF exhibits a single degradation at 450ºC, when the polymer loses more than 80% of its weight before 500ºC is reached [43]. At higher temperatures, oxidation of C into CO and CO_2 leads to additional weight loss of between 600ºC and 700˚C.

Table 4: The %wt of major elements in the untreated and pyrolyzed samples.

		%w						
T (°C)	Time (min)	Mn	Ni	Co	Cu	Li	Al	P
Untreated		11.0±0.7	5.6±0.3	5.5±0.3	12.3±0.8	2.4±0.2	6.8±0.5	0.3±0.1
400	30	11.4±0.3	6.0±0.3	5.7±0.3	12.9±0.1	2.6±0.3	7.1±0.3	0.3±0.1
	60	11.6±0.2	6.2±0.3	5.8±0.1	13.1±0.2	2.6±0.1	7.3±0.1	0.3±0.3
	90	11.8±0.2	6.3±0.3	5.9±0.3	13.4±0.3	2.7±0.3	7.4±0.3	0.3±0.2
500	30	11.7±0.3	5.9±0.3	5.7±0.3	13.0±0.3	2.8±0.2	6.0±0.3	0.3±0.1
	60	12.8±0.5	6.1±0.3	6.3±0.3	13.4±0.2	2.8±0.3	7.1±0.2	0.3±0.1
	90	13.2±0.3	6.7±0.3	6.6±0.3	15.3±0.1	3.1±0.3	7.5±0.3	0.3±0.2
600	30	11.7±0.2	6.2±0.3	5.7±0.3	12.5±0.1	2.7±0.2	7.4±0.3	0.3±0.1
	60	12.6±0.1	6.3±0.1	6.1±0.1	13.6±0.2	2.4±0.3	7.3±0.3	0.4±0.1
	90	13.2±0.3	6.7±0.3	6.6±0.3	14.4±0.3	3.1±0.3	9.9±0.3	0.4±0.1
700	30	12.0±0.1	6.5±0.1	5.9±0.1	13.6±0.3	2.9±0.1	8.2±0.1	0.4±0.1
	60	12.2±0.1	7.0±0.3	6.2±0.3	14.3±0.1	3.0±0.3	10.1±0.1	0.4±0.2
	90	14.2±0.3	7.1±0.2	6.7±0.3	15.1±0.3	3.0±0.3	10.3±0.2	0.4±0.1

Figure 22 shows the variation in the equilibrium amount versus temperature for each species involved in the carbothermic reaction of $LiCoO_2$ with C, giving Co, Li_2CO_3, and gases (CO and CO_2) as products, as described by (11). These curves are the result of thermodynamic calculations. The data shows that, above 500˚C, C forms both CO and CO_2 and the amount of CO grows with increase in temperature. This means that at 700˚C, the quantity of C consumed to form CO and CO_2 is significantly higher than at lower temperatures. Furthermore, the reactions that have these gases as products are promoted by the constant flow of nitrogen, removing CO and CO_2 from the system, which gives a situation that does not permit the reaction equilibrium to be attained.

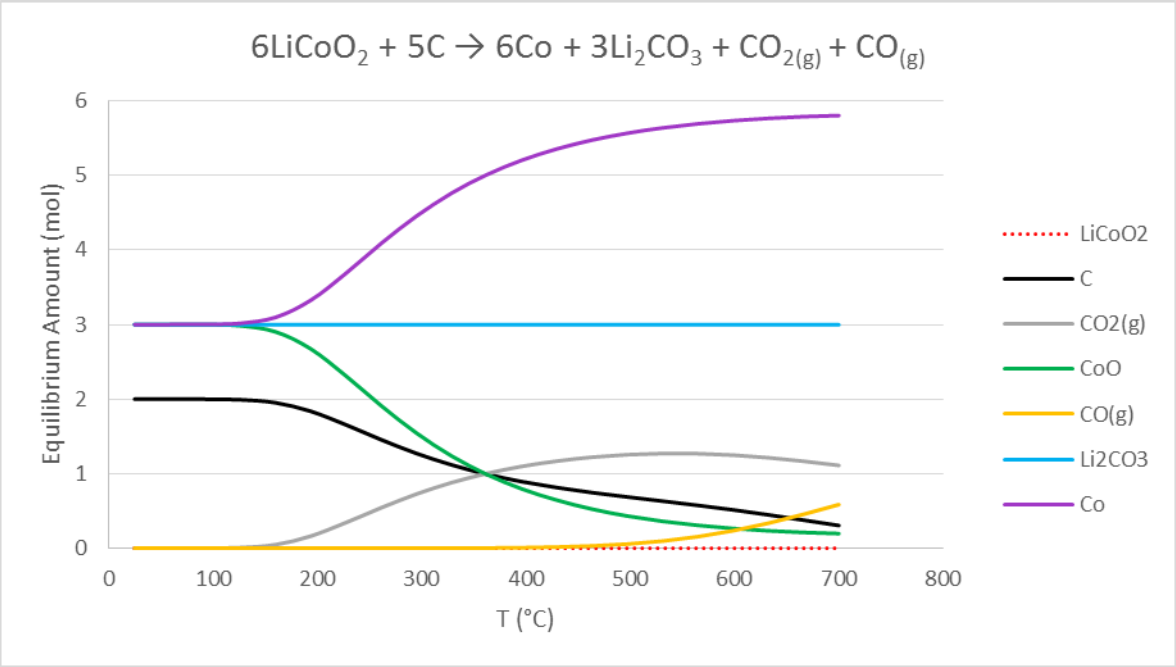

Figure 22: The variation of the equilibrium amount vs temperature for each species involved in the carbothermic reaction of $LiCoO_2$ with C, giving Co, Li_2CO_3, and gases (CO and CO_2) as products, as described by (10).

It is possible to calculate a mass balance for each element considering the weight of the samples before and after treatment, showed in Figure 18, and the data reported in Table 4. In Table 5 the quantity in $g*10^{-2}$ of each element in the treated and untreated samples is shown.

Table 5: Weight of each element in the pyrolysed and untreated samples in grams.

		Weight($g*10^{-2}$)						
T (°C)	Time (min)	Mn	Ni	Co	Cu	Li	Al	P
Untreated		5.5 ± 0.4	2.8 ± 0.2	2.8 ± 0.2	6.2 ± 0.4	1.2 ± 0.1	3.4 ± 0.3	0.2 ± 0.1
400	30	5.3 ± 0.2	2.8 ± 0.2	2.7 ± 0.2	6.0 ± 0.1	1.2 ± 0.1	3.3 ± 0.2	0.1 ± 0.0
	60	5.3 ± 0.1	2.8 ± 0.1	2.6 ± 0.1	5.9 ± 0.2	1.2 ± 0.1	3.3 ± 0.1	0.1 ± 0.1
	90	5.2 ± 0.1	2.8 ± 0.1	2.6 ± 0.1	5.9 ± 0.2	1.2 ± 0.1	3.3 ± 0.2	0.1 ± 0.1
500	30	5.3 ± 0.2	2.7 ± 0.1	2.6 ± 0.1	5.9 ± 0.2	1.3 ± 0.1	2.7 ± 0.1	0.1 ± 0.0
	60	5.6 ± 0.3	2.7 ± 0.1	2.8 ± 0.1	5.9 ± 0.2	1.2 ± 0.1	3.1 ± 0.1	0.1 ± 0.0
	90	5.6 ± 0.2	2.8 ± 0.1	2.8 ± 0.1	6.5 ± 0.2	1.3 ± 0.1	3.2 ± 0.1	0.1 ± 0.1
600	30	5.3 ± 0.1	2.8 ± 0.1	2.6 ± 0.1	5.7 ± 0.1	1.2 ± 0.1	3.4 ± 0.2	0.1 ± 0.0
	60	5.5 ± 0.1	2.8 ± 0.1	2.7 ± 0.1	5.9 ± 0.2	1.0 ± 0.1	3.2 ± 0.2	0.2 ± 0.0
	90	5.3 ± 0.2	2.7 ± 0.1	2.7 ± 0.1	5.8 ± 0.2	1.3 ± 0.1	4.0 ± 0.2	0.2 ± 0.0
700	30	5.3 ± 0.1	2.9 ± 0.1	2.6 ± 0.1	6.0 ± 0.2	1.3 ± 0.1	3.6 ± 0.1	0.2 ± 0.0
	60	5.2 ± 0.1	3.0 ± 0.1	2.6 ± 0.1	6.0 ± 0.1	1.3 ± 0.1	4.3 ± 0.1	0.2 ± 0.1
	90	5.5 ± 0.2	2.8 ± 0.1	2.6 ± 0.1	5.9 ± 0.2	1.2 ± 0.1	4.0 ± 0.1	0.2 ± 0.0

No significant differences are observed among the samples. There result indicate that during the process there is no formation of metal volatile species.

4.6.2 Incineration

Increase in temperature and length of treatment promotes the oxidation of the carbon content, which determines a rise in the concentration of metals in the samples (Table 6). Comparing the untreated sample with the sample treated at 700°C for 1.5h, it can be observed that the concentration increased by ~38%. Thus, as expected, the rise in the concentration of metals was almost proportional to the decrease in the weight of the sample (~35%).

the decrease in the weight of the samples treated at 700˚C and 600˚C stopped at a treatment time of 60 minutes, as shown in Figure 18. This can also be seen in Table 6, where the abundance of the metals in these treatment conditions did not vary significantly.

Table 6: The %wt of major elements in the untreated and incinerated samples.

		Weight %						
T (°C)	Time (min)	Mn	Ni	Co	Cu	Li	Al	P
Untreated		11.0±0.7	5.6±0.3	5.5±0.3	12.3±0.8	2.4±0.2	6.8±0.5	0.3±0.1
400	30	12.2±0.1	6.2±0.1	6.1±0.1	14.2±0.1	2.6±0.1	7.0±0.1	0.3±0.1
	60	12.8±0.2	6.3±0.2	6.5±0.1	15.4±0.1	2.6±0.1	7.9±0.2	0.3±0.1
	90	13.2±0.2	6.5±0.2	6.4±0.2	15.6±0.5	2.7±0.1	7.7±0.4	0.3±0.1
500	30	12.9±0.2	6.8±0.1	6.2±0.4	15.6±0.3	2.7±0.1	7.9±0.3	0.3±0.1
	60	13.1±0.2	6.9±0.2	6.6±0.3	15.9±0.4	3.4±0.1	8.1±0.5	0.4±0.1
	90	14.3±0.2	6.9±0.1	6.8±0.1	16.9±0.3	3.6±0.1	8.7±0.2	0.4±0.1
600	30	13.4±0.2	6.8±0.2	6.3±0.1	15.3±0.5	2.6±0.1	7.4±0.1	0.4±0.1
	60	13.8±0.3	7.6±0.1	6.6±0.5	16.6±0.3	2.8±0.1	8.0±0.4	0.4±0.1
	90	14.2±0.3	7.5±0.2	7.3±0.1	16.9±0.1	3.8±0.1	8.8±0.1	0.4±0.1
700	30	13.9±0.2	6.9±0.1	6.8±0.1	16.3±0.2	2.9±0.1	8.7±0.3	0.4±0.1
	60	14.2±0.3	7.4±0.1	7.3±0.3	16.5±0.1	2.9±0.1	9.7±0.5	0.4±0.1
	90	15.0±0.4	7.7±0.1	7.6±0.1	17.0±0.5	3.2±0.1	9.8±0.3	0.4±0.1

In Table 7 is shown how the amount in g*10^{-2} of each element varies in the samples.

*Table 7: Weight in g*10-2 of each element in the untreated and treated in presence of oxygen samples.*

		Weight(g*10^{-2})						
T (°C)	Time (min)	Mn	Ni	Co	Cu	Li	Al	P
Untreated		5.5 ± 0.4	2.8 ± 0.2	2.8 ± 0.2	6.2 ± 0.4	1.2 ± 0.1	3.4 ± 0.3	0.2 ± 0.1
400	30	5.5 ± 0.1	2.8 ± 0.1	2.7 ± 0.1	6.3 ± 0.1	1.2 ± 0.1	3.1 ± 0.1	0.1 ± 0.0
	60	5.6 ± 0.2	2.8 ± 0.1	2.9 ± 0.1	6.8 ± 0.2	1.1 ± 0.1	3.5 ± 0.1	0.1 ± 0.0
	90	5.6 ± 0.2	2.7 ± 0.1	2.7 ± 0.1	6.6 ± 0.3	1.1 ± 0.1	3.2 ± 0.2	0.1 ± 0.0
500	30	5.3 ± 0.2	2.8 ± 0.1	2.6 ± 0.2	6.4 ± 0.2	1.1 ± 0.0	3.3 ± 0.1	0.1 ± 0.0
	60	5.3 ± 0.2	2.8 ± 0.1	2.7 ± 0.1	6.4 ± 0.2	1.4 ± 0.1	3.3 ± 0.2	0.2 ± 0.0
	90	5.5 ± 0.2	2.6 ± 0.1	2.6 ± 0.1	6.5 ± 0.2	1.4 ± 0.1	3.3 ± 0.1	0.2 ± 0.0
600	30	5.2 ± 0.2	2.7 ± 0.1	2.5 ± 0.1	6.0 ± 0.2	1.0 ± 0.0	2.9 ± 0.1	0.2 ± 0.0
	60	5.1 ± 0.2	2.8 ± 0.1	2.4 ± 0.2	6.1 ± 0.2	1.0 ± 0.0	2.9 ± 0.2	0.1 ± 0.0
	90	5.1 ± 0.2	2.7 ± 0.1	2.6 ± 0.1	6.1 ± 0.2	1.4 ± 0.1	3.2 ± 0.1	0.1 ± 0.0
700	30	4.8 ± 0.2	2.4 ± 0.1	2.3 ± 0.1	5.6 ± 0.2	1.0 ± 0.0	3.0 ± 0.1	0.1 ± 0.0
	60	4.6 ± 0.2	2.4 ± 0.1	2.4 ± 0.1	5.4 ± 0.2	0.9 ± 0.0	3.2 ± 0.2	0.1 ± 0.0
	90	5.1 ± 0.2	2.6 ± 0.1	2.6 ± 0.1	5.8 ± 0.2	1.1 ± 0.0	3.3 ± 0.1	0.1 ± 0.0

It is possible to observe a significant discrepancy of the quantity of Mn, Co, and Ni between the samples untreated and treated at 700°C for 30 and 60 minutes, which equals to ~0.8 for Mn and ~0.4 for Co and Ni. This variation can be determined by the formation of volatile species, as carbonyls, through the reactions of the metal oxides with C in presence of O_2, according to the reactions (47)- (52). The analyses of the carbonyls can be performed by FTIR or gas chromatography and will be the object of future works.

4.7 XRD qualitative analysis of crystalline compounds

4.7.1 Pyrolysis

The effects of pyrolysis on the black mass crystalline compounds were studied by x-ray diffraction analysis. The presence of CO and CO_2 in the off-gas confirms that a carbothermic process took place and the XRD results show that the reduction of the oxides has modified the microstructural composition of the samples. In Figure 23, the XRD spectrum of the untreated battery is compared with the spectra for the samples treated for 1.5 h.

Making quantitative assumptions based on these spectra is not correct, but it is evident that an increase in the treatment temperature leads to a decrease in the intensity of the peaks at 26.5°, 43.3 °, and 54.9°, which represent the signals emitted by the graphitic carbon.

A carbon analyser was used to quantify the residual carbon in the samples. The sources of carbon are the graphite coating the anode layer, the separator polymer, the PVDF and the organic components of the electrolyte. The percentage weight of carbon as a function of the length of heat treatment is shown in Table 8. The carbon content in the samples treated at 700°C for 90 minutes was the lowest (16 w%), starting from an initial content of 41w%. It is probable that this weight loss was caused by consumption of the graphite and the organic substances during heating with the formation of volatile species, CO and CO_2.

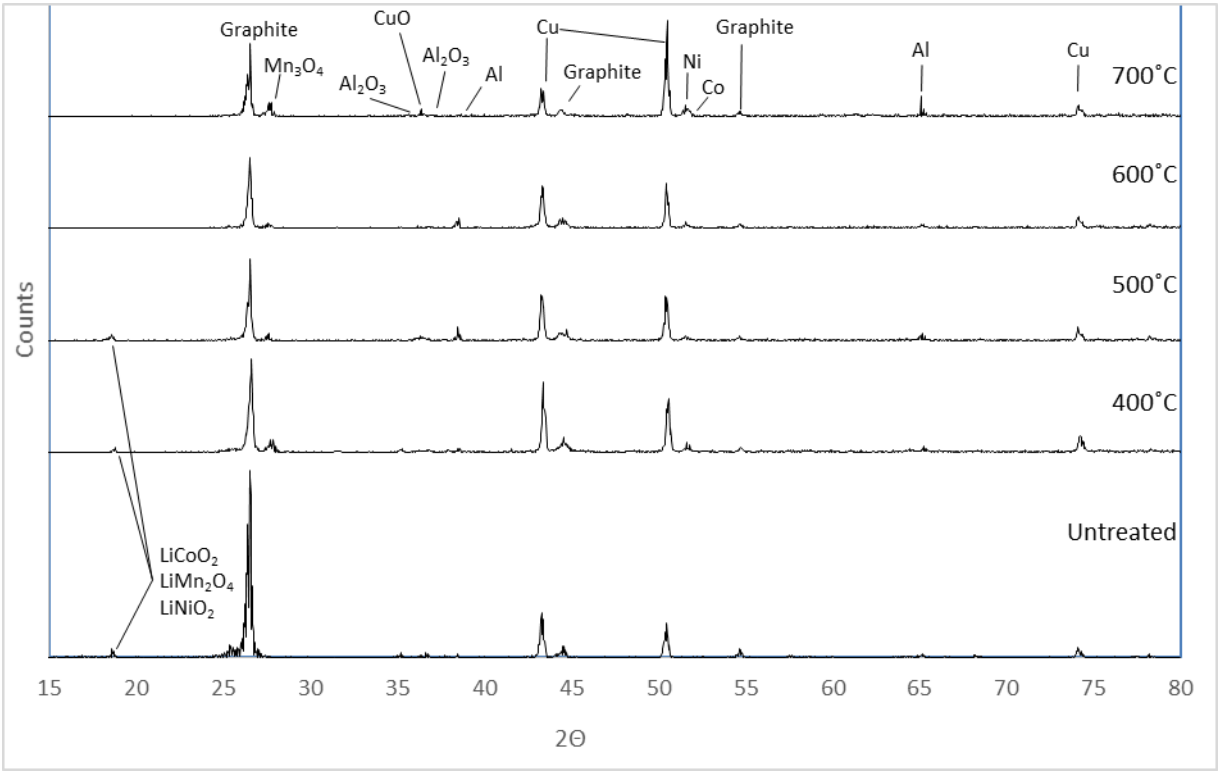

Figure 23: Comparison between the XRD spectra of an untreated sample and the spectra of samples pyrolyzed for 1.5 h at 400°C, 500°C, 600°C and 700°C.

Table 8: Variation of carbon concentration in the pyrolyzed sample with temperature for the three heat treatment periods: 30, 60, and 90 minutes.

T (°C)	time	Carbon content (%)
Untreated		40.8±2.8
400	30 min	35.5± 2.4
	60 min	32.8±2.0
	90 min	21.2±1.6
500	30 min	32.0±2.5
	60 min	31.7±2.5
	90 min	23.3±1.2
600	30 min	31.4±1.7
	60 min	29.4±2.5
	90 min	21.1±1.6
700	30 min	27.2±2.5
	60 min	25.2±0.6
	90 min	16.0±1.6

The XRD peaks at 50.5° and 74° indicate the presence of metals in elemental form, such as Ni, Cu, and Co, formed by the reducing action of the carbon on the metal oxides.

The diffraction peak at 18.7˚, which is common for all three lithium-metal oxides, is present in the diffractogram for the sample treated at 500°C, but it was not detected for the samples treated at higher temperatures (Figure 23). As shown in Figure 24, it is possible to observe the effect of increasing length of treatment: at 700°C, only after 1.5 hours, the peak at 18.7˚ disappears. Treatment at 600°C and 700°C for 1.5 hours seems to be sufficient to obtain the almost complete carbothermic reduction of the active material.

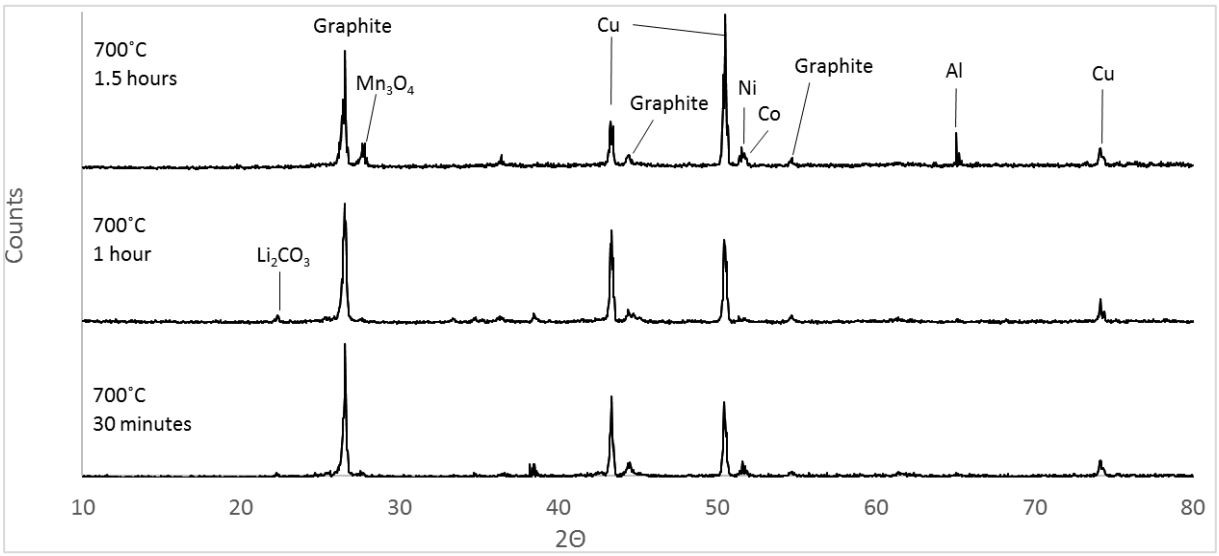

Figure 24: Comparison between XRD spectra of pyrolyzed samples at 700°C for 30 minutes, 1 hour and 1.5 hours.

The metal species have diffraction peaks at similar 2Θ angles and this limits the data resolution. To obtain a better identification of the compounds, XRD spectra of standard samples, i.e. pure metal oxides, which had been mixed with graphite and treated in pyrolysis at 700°C, were collected (Figure 25).

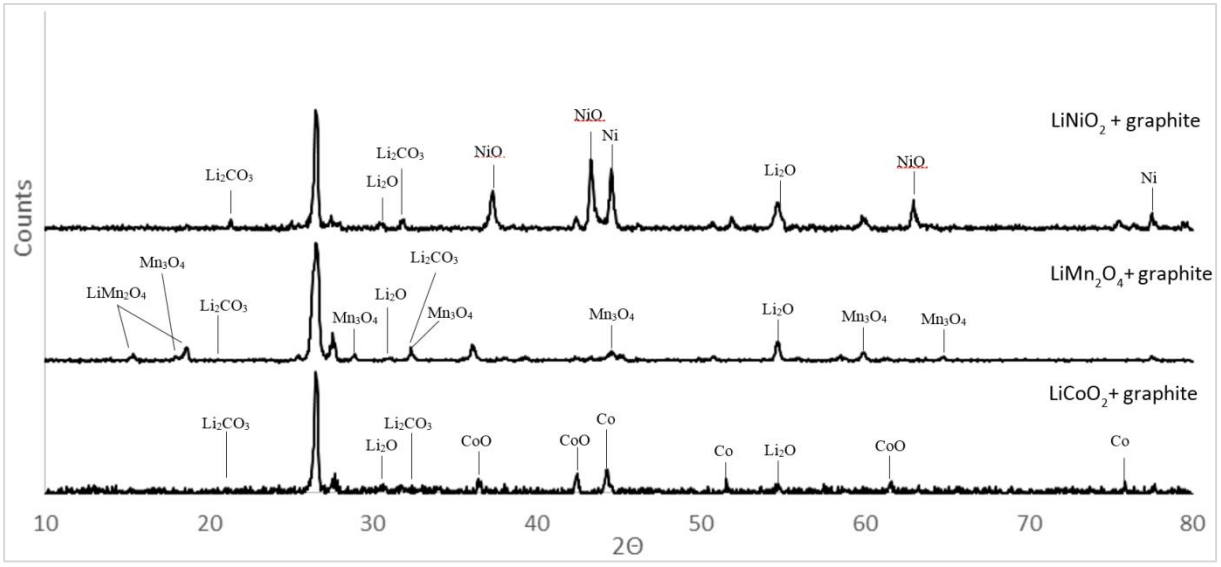

Figure 25: Comparison of XRD spectra for standard samples, consisting of a mixture of graphite and one of the oxides ($LiCoO_2$, $LiMn_2O_4$, and $LiNiO_2$.) Pyrolyzed at 700°C for 1.5 h.

The XRD spectrum of the mixture of $LiCoO_2$, pyrolyzed with excess graphite at 700°C for 1.5 h, indicates the presence of Li_2O, Li_2CO_3, CoO, and Co. This data confirms that the reactions (9) and (10) correctly describe the carbon induced reduction. The presence of Li_2O and CoO was not expected: even if the reduction of CoO to metal Co by C and CO, described by reactions (6) and (7), is permitted thermodynamically, there was not a complete transformation in the experiments. The same was observed for the reactions of Li_2O, which did not completely react with CO_2 to form Li_2CO_3 as described by reaction (8). The reason might be that the reaction time was shorter than needed (kinetic hindering) and/or that the gas flow transporting CO and CO_2 out of the system is too high, limiting the contact between the gas and the solid. Another reason is that the samples are a heterogeneous mixture of anodes and cathodes, so carbon is not equally distributed in each part of the samples.

The XRD results obtained for the reaction products from pyrolysis of a mixture of $LiMn_2O_4$ and graphite show the presence of Li_2O, Li_2CO_3, and Mn_3O_4. Also, in this case the thermodynamic considerations were confirmed and reactions (11)-(16) can be used to describe the reaction mechanism.

The XRD spectra of $LiNiO_2$ confirms that the reaction with CO and CO_2 determines the reduction to NiO and Ni, as described by (22) and (23), and the formation of Li_2O and Li_2CO_3. The time and temperature of treatment did allow the complete decomposition of NiO into Ni and the reaction between the total amounts of Li_2O with CO_2.

4.7.2 Incineration

Figure 26 shows the XRD spectrum for the untreated battery compared with the spectra for samples heat treated for 1.5 hours. The intensity of the peaks at 26.5°, 43.25°, and 54.9°, which represent the diffraction patterns for the graphitic carbon, clearly decrease with the rise in the treatment temperature. The graphite signals almost disappear after 1.5 h of treatment at 700°C. In these conditions, the graphite and organic substances are probably totally consumed during heating, with the formation of volatile species.

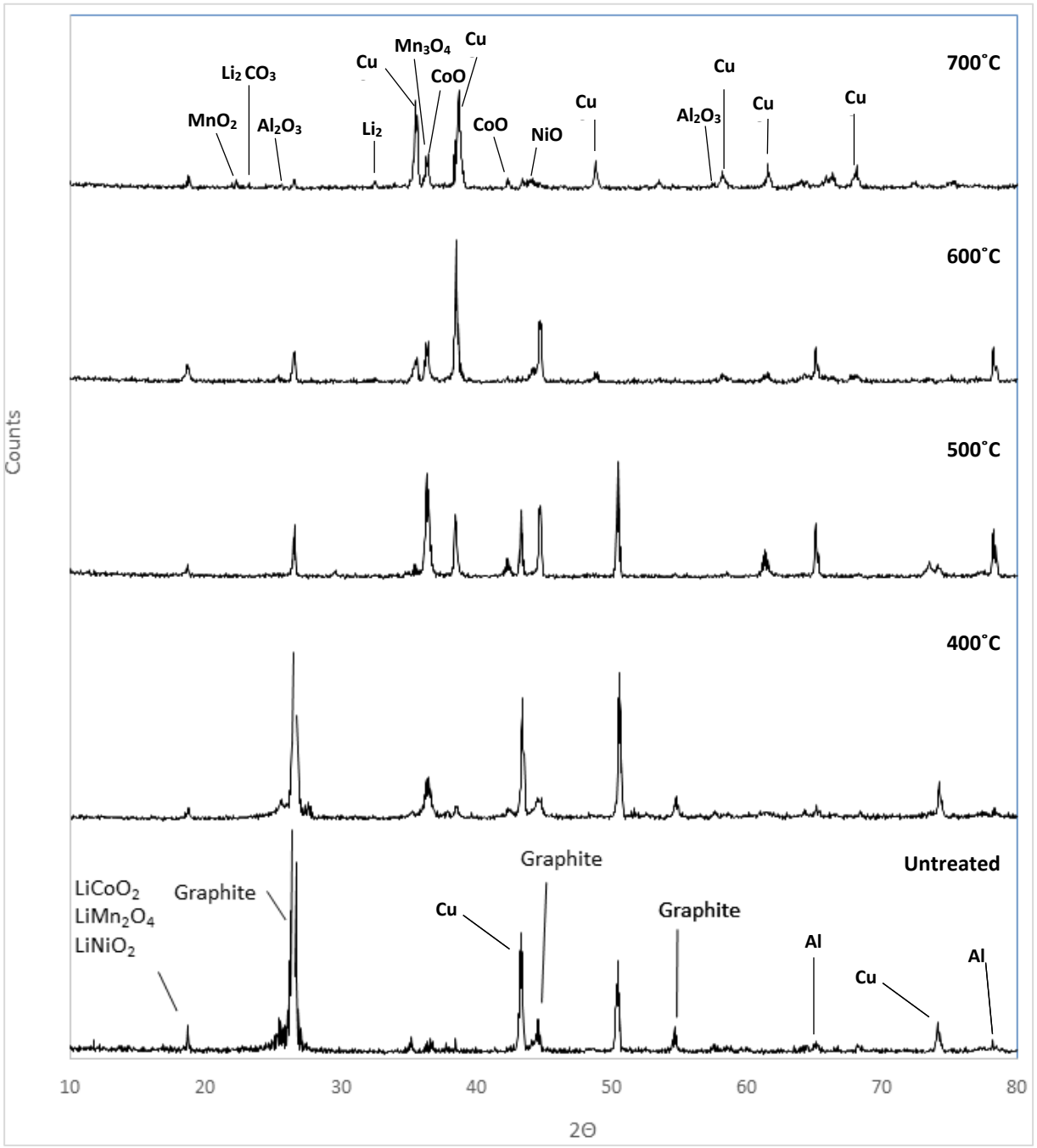

Figure 26: Comparison between the XRD spectrum of an untreated sample and the XRD spectra of the samples incinerated 1.5 h at 400°C, 500°C, 600°C, and 700°C.

To confirm this hypothesis, the residual carbon content in the samples was measured.
The data in Table 9 show that the carbon content is less than 1% after treatment at 700°C for 1.5 h, from an initial 41% in the untreated battery. It is clear that the incineration has almost completely removed the organic components.

Table 9: Variation in the carbon content in the sample versus the reaction time..

T (°C)	time	Carbon content (%)
Untreated		40.8±2.8
400	30 min	29.6±1.4
	60 min	25.0±1.5
	90 min	19.1±2.3
500	30 min	24.0±2.2
	60 min	21.5±1.2
	90 min	15.7±1.2
600	30 min	16.0±1.3
	60 min	11.9±1.0
	90 min	5.5±1.0
700	30 min	5.3±0.9
	60 min	2.2±0.2
	90 min	0.6±0.2

The air flow causes oxidation of the Cu foil. The two strong peaks at 2Θ 35.5 and 38.7 degrees correspond to the most prominent diffraction peaks for CuO:

$$2Cu(s) + O_2(g) \rightarrow 2CuO(s) \quad (54)$$

The signal at 2Θ=18˚, common for all three lithium-metal oxides, was observed for samples treated at all temperatures, which shows that it was not possible to obtain complete decomposition of these species during treatment. This is probably due to the kinetics for the oxidation of carbon compared to the kinetics of the carbothermic reduction. The presence of O_2 gives rapid incineration of the C, limiting its reaction with the metal oxides. Some of the products of the carbothermic reduction reaction were detected: CoO, MnO_2, Mn_3O_4, and NiO. In order to perform a better identification of the signals, XRD spectra of standard samples were collected for reference (Figure 27).

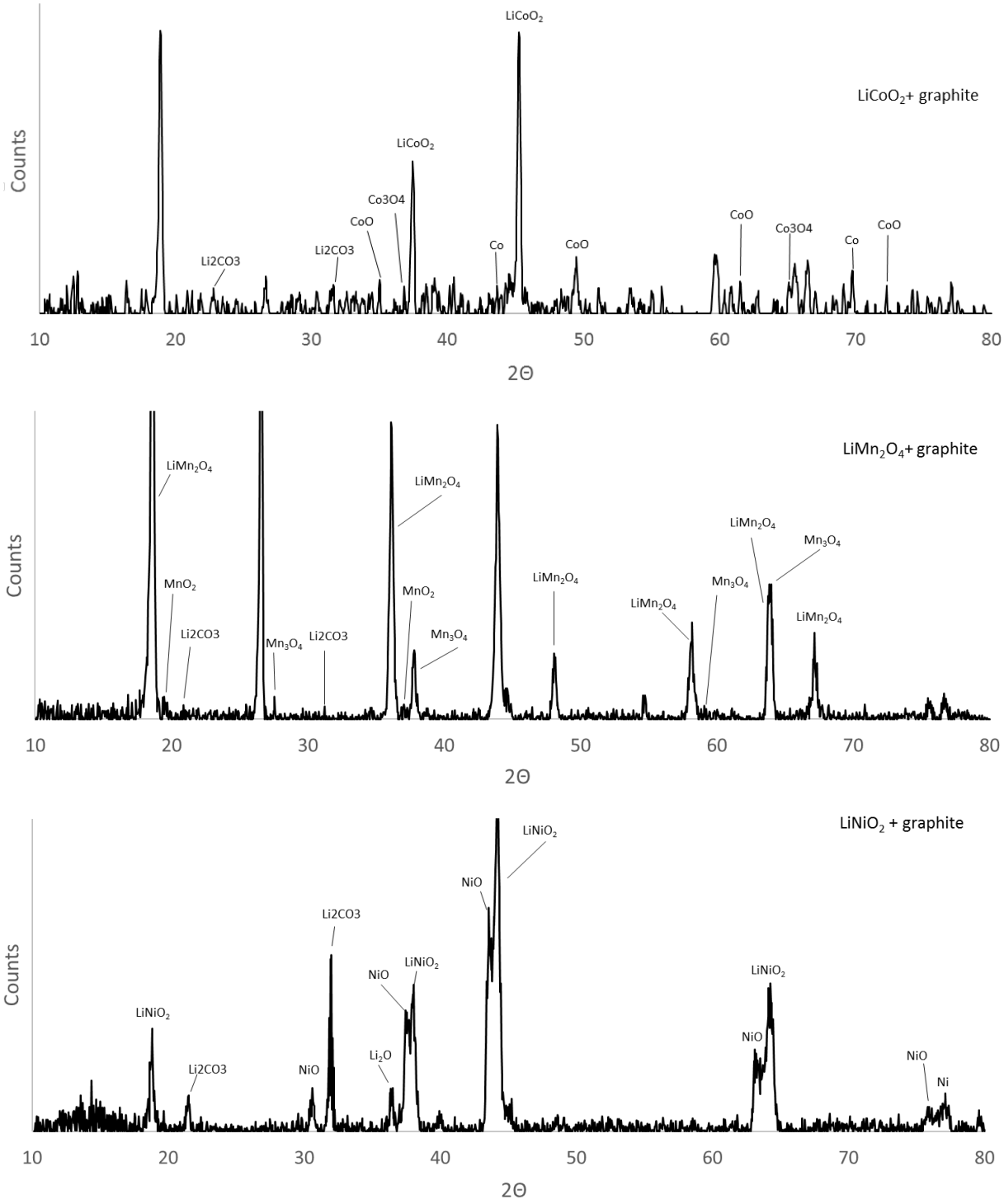

Figure 27: Comparison of the XRD diffractograms for standard samples, composed of a mixture of graphite and one of the oxides ($LiCoO_2$ (a), $LiMn_2O_4$ (b), and $LiNiO_2$ (c) Incinerated at 700°C for 1.5 h.

Incineration at 700°C for 1.5 h, with an excess of graphite, gave rise to the decomposition of $LiCoO_2$ into Li_2O, Li_2CO_3, CoO, Co_3O_4, and Co, as was expected from the thermodynamic considerations. CoO and Co_3O_4 were still present; this could be due to too short a treatment

time, which did not allow complete reduction to Co, or oxidation of part of the Co formed, by reaction with O_2, as shown in (55) and (56).

$$2Co(s) + O_2(g) \rightarrow 2CoO(s) \quad (55)$$

$$3Co(s) + 2O_2(g) \rightarrow 2\ Co_3O_4(s) \quad (56)$$

The trend of ΔG^0 as a function of T is shown in Figure 28.

The presence of Li_2O was not expected: the reactions with CO_2 should form Li_2CO_3, according to reaction (8). The reason for Li_2O still being present after the treatment might be the reaction kinetics and the presence of the gas flow, taking the CO_2 out of the system and, thus, limiting its contact with Li_2O. The X-ray diffractogram of the $LiNiO_2$ in Figure 28 shows that the reaction with C and O_2 gives Li_2O, Li_2CO_3, NiO, and Ni as its products. Similar to the results obtained with the Co-containing compounds, the presence of NiO may be due to oxidation of part of the Ni formed, (57).

$$2Ni(s) + O_2(g) \rightarrow 2NiO(s) \quad (57)$$

$LiMn_2O_4$ decomposed into MnO_2 and Mn_3O_4. No reduction of the manganese in MnO_2 to form MnO, as described by the reactions (37) and (38), could be observed.

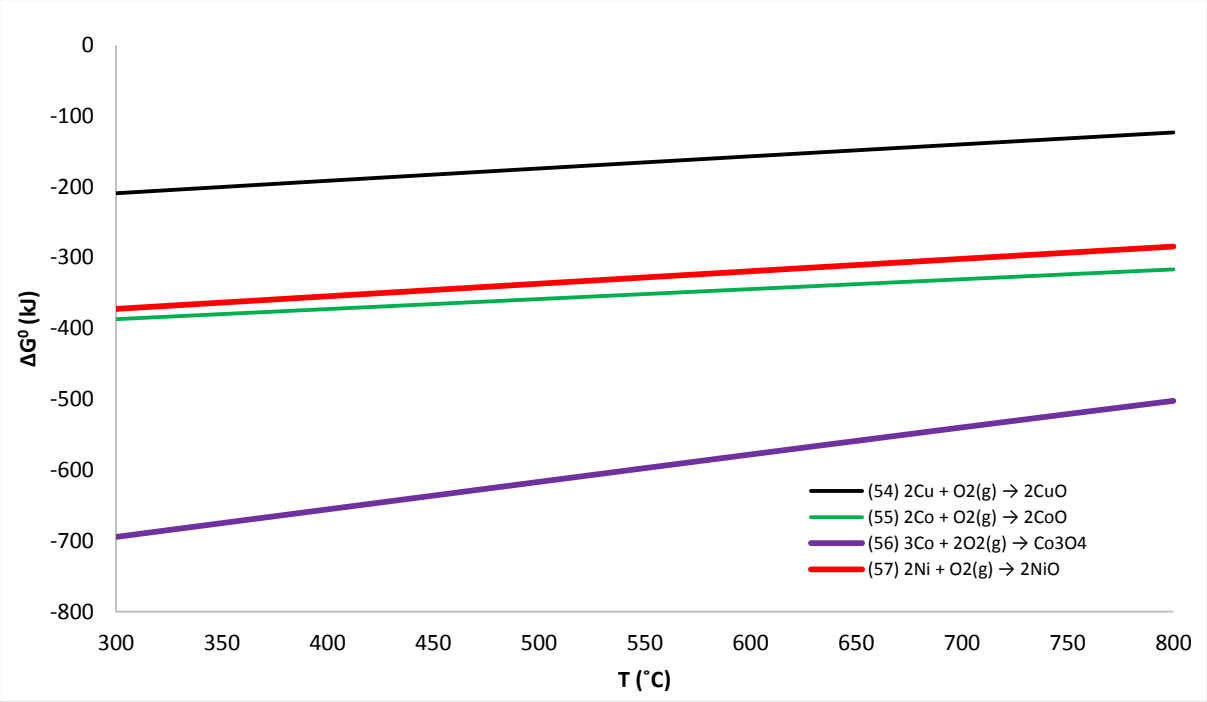

Figure 28: Plot of ΔG0 (kJ) as a function of T (°C) for the oxidation reactions of Cu, Co, and Ni.

4.8 Mechanical separation of the black mass from the foils

After the thermal pre-treatment, the effectivity of black mass removal from the foils was studied. It was observed that the high temperature had affected the mechanical properties of the samples. The Al layers were more fragile following the heat treatment. It was also easier to remove the black mass and graphite from the surface of the foils, even by hand. Thus, mechanical treatment in a ball mill was tested to remove the active material completely after the thermal treatment; in this way, copper and aluminium could be separated from the black mass.

The samples of the cathodes were placed in the furnace for 1.5 hours at 600 and 700°C. The aluminium foils were particularly fragile after treatment at 700°C and the product from the milling was a powder composed of both aluminium and active material, making their separation difficult.

On the other hand, it was possible to obtain aluminium and copper layers well separated from the active material from the samples treated at 600°C, as shown in Figure 29.

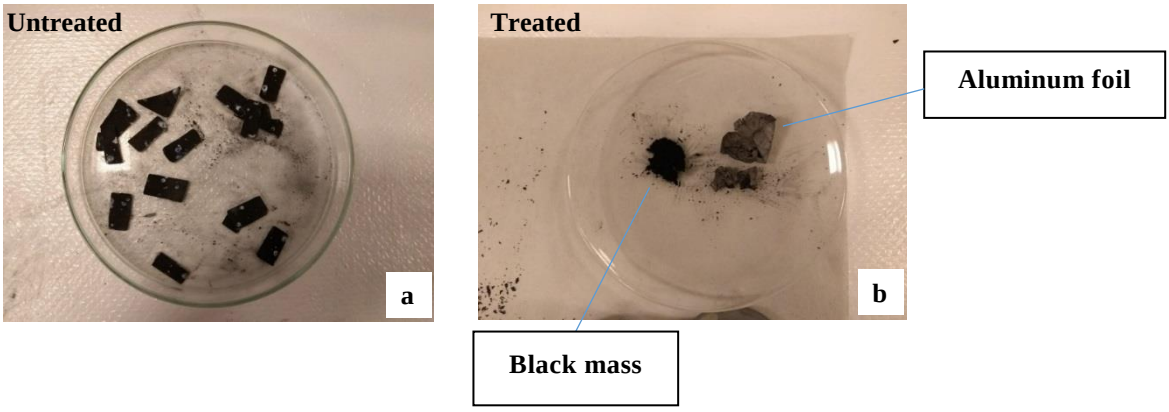

Figure 29: (a) Untreated samples subjected to mechanical treatment, (b) thermally treated samples subsequently subjected to the mechanical treatment.

The cathode's active material represents approximately 85% of the weight of a single untreated cathode. For the pyrolyzed samples, after 10 minutes of milling, it was possible to separate a quantity of active material from the aluminium layer, equal to 74.9% ± 4.8 of the weight of the treated cathodes, and 77.2% ± 4.1 of the active materials, after 30 minutes of milling. For the incinerated samples, this was 72.9% ± 2.7 after 10 minutes and 78.3% ± 1.3 after 30 minutes of milling (Table 10).

Table 10: Black mass recovered after 10 and 30 minutes of milling (%) from the untreated, pyrolysed and incinerated cathode samples.

	Average black mass recovered after milling (%)	
	10 minutes of milling	30 minutes of milling
Untreated	2.5 ± 0.2	2.8 ± 0.4
Pyrolysis	74.9 ± 4.8	77.2 ± 4.1
Incineration	72.9 ± 2.7	78.3 ± 3.3

The comparison with the untreated samples shows the efficiency of the thermal treatment: after 10 minutes in the mill, the quantity of material removed from the treated cathodes is 25 times higher than the quantity obtained from the untreated ones.

It was thus verified that thermal treatment followed by a mechanical one permits the separation of graphite and black mass from the metal foils. This is probably due to the decomposition at high temperature of the polymers, such as PVDF, which acts as a glue between the metal layers and the active material.

It could be advantageous for the subsequent hydrometallurgical treatment to prevent the presence of Cu and Al in the treatment. Since these metals can be recovered separately, the leaching and solvent extraction steps can be focused on the recovery of Co, Mn, Ni and Li. This reduces the number of process steps needed in this part of the recycling process.

5. Conclusions

The effects of pyrolysis and incineration on the composition of a mixture of cathode and anode materials from an NMC-LiB have been studied.

It was observed that during treatment of the samples at a temperature between 400-700°C, the C triggers a carbothermic reduction of the cathode's active material. Co, Ni, and Mn compounds are reduced to a lower oxidation and/or more soluble state, and so this has the potential to improve the leaching efficiency.

During the pyrolysis, Co, Mn, and Ni are obtained in a lower oxidation and/or more soluble state. Co, CoO, Ni, NiO, Mn, Mn_3O_4, Li_2O, and Li_2CO_3 are the main products. During incineration, a partial oxidation of the products from the decomposition of the lithium-metal-oxide was observed. Co, CoO, Co_3O_4, Ni, NiO, Mn_3O_4, and MnO_2 were formed. Li stayed in the oxidation state +1 and formed Li_2O, and Li_2CO_3. The O_2 in the gas flow causes some oxidation of the Cu and Al foils, with the formation of CuO and Al_2O_3. The oxidation of the Cu and Al metal foils may introduce the need for extra steps in the hydrometallurgical recovery of valuable elements following the thermal treatment described in this work.

On performing the pyrolysis at 600˚C for 90 minutes, the signal of the lithium-metal-oxides disappears in the XRD diffractogram due to complete decomposition of these oxides. The increase in temperature and length of treatment promotes the carbothermic reduction and the removal of graphite and organic components. It was observed that during pyrolysis at 700°C for 90 minutes, the carbon content reached 16 w%, starting from an initial 41w%. The data show that incineration performed under the same conditions causes the almost complete decomposition of the graphite and organic species, ~1 w%. These components can decrease the efficiency of the leaching and solid-liquid separation processes, because of their hydrophobicity, so this thermal treatment could be used to simplify and improve the hydrometallurgical recycling of metals from LiBs.

The organic components decompose during treatment releasing the gas produced, composed mainly of CO_2, CO, and H_2O. The PVDF decomposes during treatment releasing HF, in the gaseous state, and an organic by-product rich in fluorine. The decomposition of the binder enabled the efficient separation of the electrode's active material from the metal layers by means of mechanical treatment in ball mill.

The method we have performed can be applied flexibly to batteries with different chemistries. Pyrolysis is already used as a thermal pre-treatment in some industrial recycling processes. The results of this work can be useful for the optimization of these currently used processes or offer useful information for the development of more sustainable processes in the future on the laboratory and industrial scale. Our further work will include the development of such a flexible hydrometallurgical process for the economically convenient recovery of metals from spent LiBs with different chemistries and a more detailed analysis of the by-products generated during the thermal treatment.

6. Acknowledgments

This thesis has been carried out at Chalmers University of Technology, Department of Chemistry and Chemical Engineering. An acknowledgment goes to the Swedish Energy Agency – Battery Fund (Grant No: 40506-1) for providing the funding of this research.

A great deal of thanks is extended to:

Martina Petranikova for her patience, knowledge and invaluable help. In these years she has been always present for me as a guide with kindness and willingness.

Britt-Marie Steenari for her guidance, knowledge and the important suggestions that she has given me to make better my method of work and writing.

My examiner Christian Ekberg for his kind assistance.

Mark R.StJ. Foreman for his essential help in the analysis of the organic by-products.

Burcak Ebin for his help with experiments and his willingness to answers my incredible amount of questions.

Stellan Holgersson for his invaluable help with the laboratory equipment.

The rest of the people at NC/IMR. I feel lucky to work with and next to so incredible and talented people. A special thank to Marino Gregoric and Fredrik Espegren.

My family and friends for their support and to always be present for me despite the distance.

My girlfriend Alice for her love and support. You are the most interesting, shining and beautiful person that I have ever met.

The authors would like to acknowledge the support of Volvo Cars Corporation for providing the samples and valuable discussion.

We also thank the Department of Modeling and Simulation at Outotec for the help with the extending the database data for the thermodynamic calculations.

References

[1]. Chagnes A, Swiatowska J. Lithium Process Chemistry Resources, Extraction, Batteries, and Recycling. ELSEVIER, 2015.

[2]. International Energy Agency; Oil information: Overview; 2018. ISBN PDF: 978-92-64-30118-4.

[3]. International Energy Agency; Coal information: Overview; 8/2018; ISBN PDF: 978-92-64-30122-1.

[4]. Scrosati B, Garche J. Lithium batteries: Status, prospects and future. Journal of Power Sources. 5/2010;195(9):2419{2430. Available from: https://doi.org/10.1007/s11837-013-0666-4.

[5]. Talens Peiro L, Gara VM, Ayres RU. Lithium: Sources, Production, Uses, and Recovery Outlook. JOM. 8/013; 65(8):986-996.

[6]. International Energy Agency; Global EV outlook; 6/2017

[7]. Warner J. The Handbook of Lithium-Ion Battery Pack Design: Chemistry, Components, Types and Terminology. Elsevier, 5/2015

[8]. Report on Critical Raw Materials for the EU, Report of the Ad hoc Working Group on defining critical raw; 9/2017.

[9]. Miedema JH, Moll HC. Lithium availability in the EU27 for battery-driven vehicles: the impact of recycling and substitution on the confrontation between supply and demand until 2050. Resources Policy; 2013 38 (2) 204–211.

[10]. Moradi B, Botte GG. Recycling of graphite anodes for the next generation of lithium ion batteries. Journal of Applied Electrochemistry; 2016 46:123–148.

[11]. Watanabe C. Why Battery Cost Could Put the Brakes on Electric Car Sales. BNEF.com; 11/29/2017.

[12]. Mizushima, K, Jones P. C, Wiseman P. J, Goodenough J. B. Li_xCoO_2 ($0 < x \leq 1$): a New Cathode Material for Batteries of High Energy Density. Materials Research Bulletin. 1980, 15, 783−789.

[13]. Xu B, Qian D, Wang ZY, Meng YS. Recent progress in cathode materials research for advanced lithium ion batteries. Materials Science and Engineering: R: Reports 2012;73:51e65.

[14]. Li L, Dunn JB, Zhang XX, Gaines L, Chen RJ, Wu F, Amine K. Recovery of metals from spent lithium-ion batteries with organic acids as leaching reagents and environmental assessment. Journal of Power Sources 233 (2013) 180-189

[15]. Hanisch C, Diekmann J, Stieger A, Haselrieder W, Kwade A. Recycling of Lithium-Ion Batteries; Handbook of Clean Energy Systems; published by John Wiley & Sons, Ltd 2015.

[16]. Wakihara M, Yamamoto O. Lithium ion batteries: fundamentals and performance. Wiley-VCH; 1998. p. 127e55. ISBN:3-527-29569-0.

[17]. Romare M, Dahllöf L. The Life Cycle Energy Consumption and Greenhouse Gas Emissions from Lithium-Ion Batteries. IVL Swedish Environmental Research Institute 2017

[18]. Zhang T, He Y, Wang F, Ge L, Zhu X, Li H. Chemical and process mineralogical characterizations of spent lithium-ion batteries: an approach by multi-analytical techniques. Waste Management; 2014;34: 1051-8.

[19]. Diekmann J, Hanisch C, Froböse, Gerrit Schälicke L, Loellhoeffel T, Fölster A, Kwadea A. Ecological Recycling of Lithium-Ion Batteries from Electric Vehicles with Focus on Mechanical Processes. Journal of the Electrochemical Society (2017) 164 (1) A6184-A6191.

[20]. Peled E. The electrochemical behaviour of alkali and alkaline earth metals in nonaqueous battery systems-the solid electrolyte interphase model. Journal Electrochem Soc 1979;126:2047e51.

[21]. Gaines L. The future of automotive lithium-ion battery recycling: Charting a sustainable course. Sustainable Materials and Technologies; 1–2 (2014) 2–7.

[22]. Yazicioglu B, Tytgat J. Life cycle assessment involving Umicore ’s battery recycling process. 2014. Available at:www.batteryrecycling.umicore.com [cit. 12.01.15].

[23]. Tytgat J. Umicore battery recycling. 2014. www.batteryrecycling.umicore.com [cit. 12.01.15].

[24]. Li Z, Huang J, Liaw BY, Metzler V, Zhang J. A review of lithium deposition in lithium-ion and lithium metal secondary batteries. Journal of Power Sources 254 (2014) 168-182.

[25]. Petrániková M, Miškufová A, Havlík T, Forsén O, Pehkonen A. Cobalt Recovery From Spent Portable Lithium Accumulators After Thermal Treatment. Acta Metallurgica Slovaca, Vol. 17, 2011, No. 2, p. 106-115.

[26]. Morel H. Ultra-high temperature technology at Umicore. Available at: www.batteryrecycling.umicore.com [cit. 12.01.15].

[27]. Joulié M, Laucournet R, Billy E. Hydrometallurgical process for the recovery of high value metals from spent lithium nickel cobalt aluminium oxide-based lithium-ion batteries. Journal of Power Sources 2014; 247: 551e5.

[28]. Lain MJ. Recycling of lithium ion cells and batteries. Journal of Power Sources 2001; 97e98:736e8.

[29]. Granata G, Moscardini E, Pagnanelli F, Trabucco F, Toro L. Product recovery from Li-ion battery wastes coming from an industrial pre-treatment plant: lab scale tests and process simulations. Journal of Power Sources 2012; 206:393e401.

[30]. He LP, Sun SY, Mu YY, Song XF, and Yu JG. Recovery of Lithium, Nickel, Cobalt, and Manganese from Spent Lithium-Ion Batteries Using L‑Tartaric Acid as a Leachant. ACS Sustainable Chem. Eng. 2017, 5, 714−721

[31]. Lee CK, Rhee KI. Preparation of LiCoO2 from spent lithium-ion batteries. Journal of Power Sources 2002;109: 17e21.

[32]. Meshram P, Pandey BD, Mankhand TR. Extraction of lithium from primary and secondary sources by pre-treatment, leaching and separation: A comprehensive review. Hydrometallurgy 150 (2014) 192–208.

[33]. Lv WG, Wang ZH, Cao HB, Sun Y, Zhang Y, Sun Z. A critical review and analysis on the recycling of spent lithium-ion batteries. ACS Sustain Chem Eng 2018;6 (2):1504–21.

[34]. Petrániková M, Miškufová A, Havlík T, Forsén O, Pehkonen A. cobalt recovery from spent portable lithium accumulators after thermal treatment. Acta Metallurgica Slovaca, Vol. 17, 2011, No. 2, p. 106-115.

[35]. Paulino J, Busnardo N, Afonso J. Journal of Hazardous Materials, Vol. 150, 2008, p. 843–849.

[36]. Shin SMS, Kim NH, Sohn JS, Yang DH, Kim YH. Development of metals recovery process from Li-ion battery waste. Hydrometallurgy 2005;79:172e81.

[37]. Sun L, Qiu K. Vacuum pyrolysis and hydrometallurgical process for the recovery of valuable metals from spent lithium-ion batteries. Journal of Hazard Material 2011;194:378e84

[38]. Li J, Wang G, Xu Z. Environmentally-friendly oxygen-free roasting/wet magnetic separation technology for in situ recycling cobalt, lithium carbonate and graphite from spent LiCoO2/graphite lithium batteries. Journal of Hazardous Materials. 302 (2016) 97–104.

[39]. Xiao J, Li J, Xu Z. Recycling metals from lithium ion battery by mechanical separation and vacuum metallurgy. Journal of Hazardous Materials 338 (2017) 124–131.

[40]. Yang Y, Huang G, Xu S, He Y, Liu X. Thermal treatment process for the recovery of valuable metals from spent lithium-ion batteries. Hydrometallurgy 165 (2016) 390–396.

[41]. Knyazev AV, Ma˛czka M,. Smirnova NN, Knyazeva SS, Chernorukov NG, Ptak M, Shushunov AN. Study of the phase transition and thermodynamic functions of LiMn2O4. Thermochimica Acta 593 (2014) 58–64.

[42]. Lai C, Chen J, Knight JC, Manthiram A, Navrotsky A. Thermodynamic Stability of Transition-Metal-Substituted LiMn2-xMxO4 (M=Cr, Fe, Co, and Ni) Spinels. ChemPhysChem 2016, 17, 1973 – 1978.

[43]. Kuila A, Maity N, Chatterjee DP, Nandi K. Temperature triggered antifouling properties of poly(vinylidene fluoride) graft copolymers with tuneable hydrophilicity. Journal of Materials Chemistry A 2015, 3,13546.